Low-Level Mesovortices within Squall Lines and Bow Echoes. Part I: Overview and Dependence on Environmental Shear

MORRIS L. WEISMAN

National Center for Atmospheric Research, Boulder, Colorado*

ROBERT J. TRAPP+

Cooperative Institute for Mesoscale Meteorological Studies, University of Oklahoma, Norman, Oklahoma

(Manuscript received 12 November 2002, in final form 3 June 2003)

ABSTRACT

This two-part study proposes fundamental explanations of the genesis, structure, and implications of low-level meso-γ-scale vortices within quasi-linear convective systems (QLCSs) such as squall lines and bow echoes. Such ''mesovortices'' are observed frequently, at times in association with tornadoes.

Idealized simulations are used herein to study the structure and evolution of meso-γ-scale surface vortices within QLCSs and their dependence on the environmental vertical wind shear. Within such simulations, significant cyclonic surface vortices are readily produced when the unidirectional shear magnitude is 20 m s^{-1} or greater over a 0–2.5- or 0–5-km-AGL layer. As similarly found in observations of QLCSs, these surface vortices form primarily north of the apex of the individual embedded bowing segments as well as north of the apex of the larger-scale bow-shaped system. They generally develop first near the surface but can build upward to 6–8 km AGL. Vortex longevity can be several hours, far longer than individual convective cells within the QLCS; during this time, vortex merger and upscale growth is common. It is also noted that such mesoscale vortices may be responsible for the production of extensive areas of extreme ''straight line'' wind damage, as has also been observed with some QLCSs. Surface vortices are also produced for weaker shears but remain shallow, weak, and short-lived.

Although similar in size and strength to mesocyclones associated with supercell storms, and also sometimes producing similar hooklike structures in the rain field, it is also shown that the present vortices are quite distinct, structurally and dynamically. Most critically, such vortices are not associated with long-lived, rotating updrafts at midlevels and the associated strong, dynamically forced vertical accelerations, as occur within supercell mesocyclones.

1. Introduction

Quasi-linear convective systems (QLCSs), such as squall lines and bow echoes, represent one of the primary modes of observed convective organization and are often associated with the production of severe weather, such as heavy rainfall, hail, strong surface winds, and tornadoes. Recent observations suggest that many of the severe weather events associated with QLCSs, including both tornadoes and damaging straight-line winds, are associated in some way with the development of significant low-level meso-γ-scale (e.g., 2–40 km) vortices within such systems. These ''mesovortices'' range in scale and structure, with strengths sometimes comparable to the more commonly studied supercell mesocyclones. Observations to date, however, have been insufficient to deduce mechanisms of vortex formation or to understand their relationship to severe weather production. The goal of this two-part study is to investigate the properties of low-level vortices produced in idealized simulations of QLCSs, with the hope of clarifying their structural characteristics, mechanisms of formation, and their relationship to environmental conditions and severe weather production.

An example of the type of system being investigated in this study is presented in Fig. 1, which depicts a large bow-shaped convective system near Paducah, Kentucky, on 5 May 1996. The Doppler winds clearly depict some well-known kinematic features of bow echoes, including a rear-inflow jet (Smull and Houze 1987; Jorgensen and Smull 1993) and associated rear-inflow notch (Burgess and Smull 1990; Przybylinski 1995) behind the core of the system. Also evident is weak anticyclonic shear to

* The National Center for Atmospheric Research is sponsored by the National Science Foundation.

+ Additional affiliation: NOAA/National Severe Storms Laboratory, Boulder, Colorado.

Corresponding author address: Morris L. Weisman, NCAR, P.O. Box 3000, Boulder, CO 80307-3000.
E-mail: weisman@ncar.ucar.edu

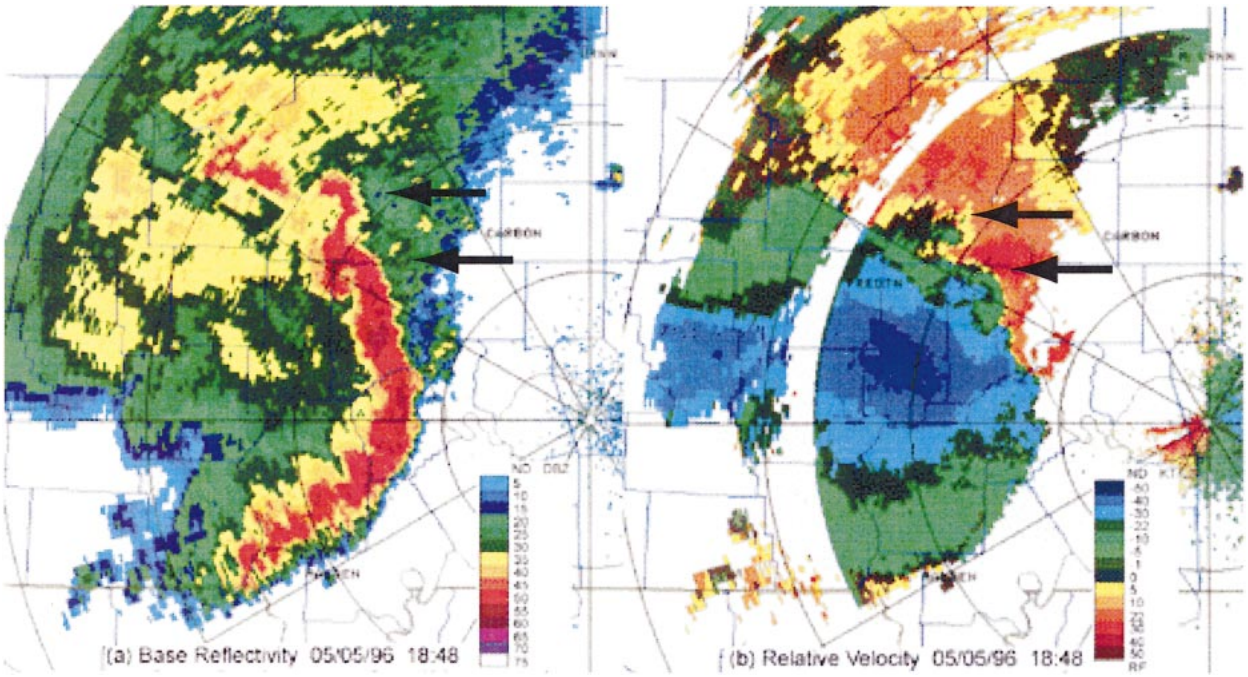

FIG. 1. (a) Base reflectivity and (b) relative velocity from the Paducah, KY, WSR-88D at 1848 UTC for 5 May 1996. Velocities are presented relative to a storm motion of 33 kts from 280°. Bold arrows indicate the locations of two embedded bow segments and associated cyclonic book-end vortices, as described in the text (R. Przybylinski 2000, personal communication).

the south of the bow and stronger cyclonic shear behind the northern end of the bow. Two smaller-scale bows are also embedded with the larger circulation, north of the system apex, with each having a localized rear-inflow jet with associated rotational features on the ends. It is such smaller-scale embedded rotational features rather than the system-scale features that are the primary emphasis of this paper.

From observational studies, one may infer a close association between the development of such mesovortices and severe weather production within such systems (e.g., Fujita 1978; Forbes and Wakimoto 1983; Wakimoto 1983; Smith and Partacz 1985; Przybylinski 1988; Przybylinski et al. 2000, 1996; Prost and Gerard 1997; Pence et al. 1998; Funk et al. 1996a,b; 1999; DeWald and Funk 2000; Miller and Johns 2000). Funk et al. (1999) discuss a severe squall line that moved across the middle Mississippi and Ohio Valleys on 15 April 1994. This system developed in an environment of strong low-level vertical wind shear (20–25 m s^{-1} of shear in the lowest 2 km AGL) and large CAPE (2400 J kg^{-1}) and included a sequence of seven embedded bowing segments, each of which produced ''straight line'' wind damage at the ground that was associated with cyclonic mesovortices; mesovortices in three of the bowing segments spawned tornadoes. According to Funk et al. (1999), ''Vortex genesis usually occurred as a low-level cyclonic-convergent area along the leading edge of the bow apex. Maturity was achieved through subsequent vortex strengthening and deepening while propagating poleward (northward) with respect to the apex. Dissipation included vortex broadening with a tendency for rearward line-relative propagation as new convective cells and low-level circulations initiated along the leading bow apex.'' They also noted that multiple circulations could exist simultaneously at different stages of development, with some of the circulations reaching the mesocyclone criteria often associated with tornadogenesis within supercells. Tornadoes tended to occur during the intensification and deepening of the low-level vortex.

DeWald and Funk (2000) documented a squall line that moved east across south-central Indiana and central Kentucky during the early morning of 20 April 1996 that contained several bowing segments, with several tornadoes embedded within the bowing segments. The environment included 3000–4000 J kg^{-1} of CAPE, with 20–30 m s^{-1} of shear in the lowest 2 km AGL, with winds continuing to increase aloft. They noted, ''Tornadogenesis occurred as transient low-level shear zones along and north of the apexes of bowing segments spun-up rapidly into well-defined, deep-layered cyclonic circulations that often met mesocyclone rotational velocity criteria.''

Miller and Johns (2000) considered nontornadic convective systems that produced what they referred to as ''extreme damaging wind'' (XDW), characterized, for example, by widespread forest blowdowns and/or severe building damage equivalent to upper-F1 (Fujita 1981) intensity. While some of these cases had the maximum surface winds near the apex of the bow echo, others had

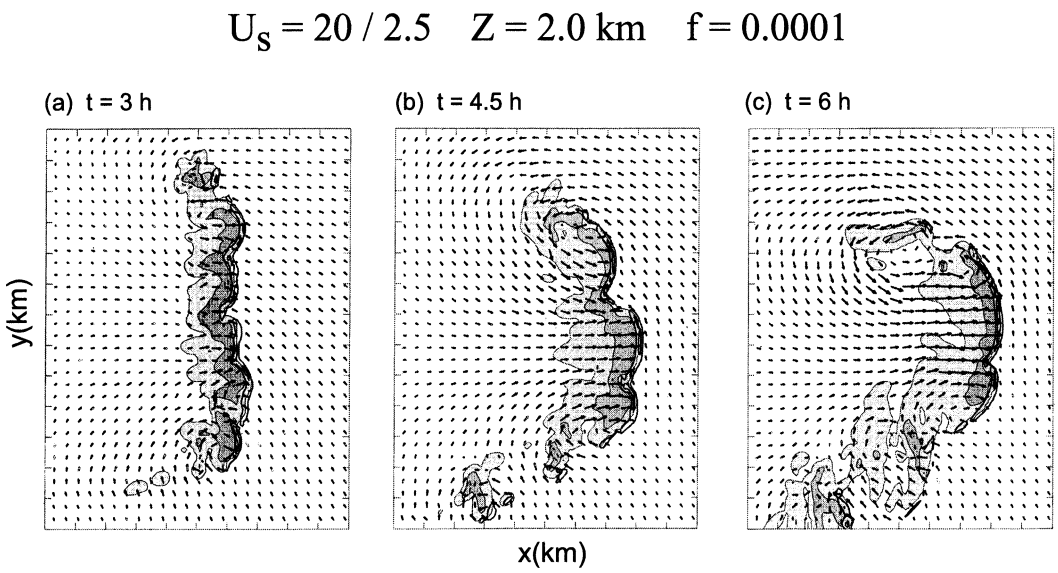

FIG. 2. Horizontal cross sections of system-relative flow, rainwater mixing ratio, and vertical velocity at 2 km AGL for the U_s = 20 m s^{-1} over 2.5 km shear simulation, with Coriolis forcing at 3, 4.5, and 6 h. Vectors are presented every four grid points (8 km), with a vector length of 8 km equal to a wind magnitude of 20 m s^{-1}. The rainwater is contoured for magnitudes greater than 1 g kg^{-1} (lightly shaded) and magnitudes greater than 3 g kg^{-1} (darkly shaded). The vertical velocity is contoured at 5 m s^{-1} intervals, with the zero contours omitted. A domain speed of u_m = 18.5 m s^{-1} has been subtracted from the flow field. Tick marks are spaced 20 km apart (adapted from Weisman and Davis 1998).

extreme winds associated with ''supercell-like'' features embedded within the line, with associated deep mesocyclonic structures, notches, or hook echoes in the rain field, etc. (e.g., Przybylinski and DeCaire 1985). One of the distinguishing features of the embedded supercell-type events was the extended duration of severe winds at a given location, sometimes greater than 20 min, as opposed to the more usual several-minute duration associated with more standard bow-echo events.

A recent study by Tessendorf and Trapp (2000) suggests that squall-line/bow-echo tornadoes account for up to 20% of all tornadic events nationwide. However, issuing appropriate severe weather warnings for such tornadoes is especially problematic. While supercells and their attendant mesocyclones and tornadoes are often observed during the organizing stages of such QLCSs (e.g., when cells are more isolated), supercells are generally not involved in the more mature stages, and, as such, there is often no readily identifiable radar precursors preceding such tornadoes with much lead time (e.g., Trapp et al. 1999). Unlike the well-known relationship between midlevel mesocyclones associated with supercell updrafts and tornadoes, a clear relationship between the midlevel line-end vortices that are located behind the active leading-line convection and above the surface cold pool and associated tornadoes has yet to be established (e.g., Funk et al. 1999).

Idealized numerical modeling studies to date have been able to reproduce much of the observed QLCS spectrum, ranging from strong, quasi-two-dimensional lines of cells, forced by deep lifting along the leading edge of a strong surface cold pool (e.g., Weisman and Klemp 1986; Rotunno et al. 1988; Weisman et al. 1988; Skamarock et al. 1994; Coniglio and Stensrud 2001) to highly organized bow echoes with strong ''book-end'' vortices and elevated rear-inflow jets (e.g., Weisman 1992, 1993; Weisman and Davis 1998, hereafter WD98; Schmidt and Cotton 1989; Bernardet and Cotton 1998). Similar to the observational studies (e.g., Johns and Hirt 1987; Evans and Doswell 2001), the environments for simulated severe convective systems generally include large CAPEs and moderate low-to-midlevel shear of at least 10–15 m s^{-1} over the lowest 2–5 km AGL. However, the more organized bow echoes require stronger shear values of at least 15–20 m s^{-1} over the lowest 2–5 km AGL.

The idealized modeling results for systems developing in the more strongly sheared environments are summarized in Fig. 2, which depicts the evolution of a finite line of convective cells over a 6-h period in the presence of Coriolis forcing in an environment of 20 m s^{-1} of vertical wind shear in the lowest 2.5 km AGL and 2200 J kg^{-1} of CAPE (WD98). The initial line of cells evolves into a strong, bow-shaped line of cells by 4 h, with near–mirror image cyclonic and anticyclonic line-end vortices evident at midlevels (also referred to as book-end vortices). The system becomes highly asymmetric by 6 h, with a dominant northern cyclonic vortex at midlevels, as is often observed (e.g., Fig. 1). In certain cases, these midlevel cyclonic vortices develop into balanced mesoscale convective vortices (MCVs; e.g., Davis and Weisman 1994). Additionally,

smaller-scale bow-shaped segments with ''subsystem scale'' dominantly cyclonic line-end vortices are observed to develop along the line, as is similarly shown by the observational example presented in Fig. 1.

While not presented or considered in WD98, significant low-level vortices are also produced in their simulations, with characteristics reminiscent of observed cases. The goal of the present study is to expand on previous work and on the studies of Weisman (1993) and WD98 to characterize the structure and evolutionary characteristics of such low-level mesovortices and to clarify the environmental conditions most conducive to their development. We will specifically show that strong vertical wind shear, especially when concentrated at low levels, is critical for the development of significant surface mesovortices. We will also clarify the relationship of these features to the midlevel line-end or book-end vortices that also often accompany such systems. We do not consider here lines of individual supercells, which become more prevalent in stronger or deeper shears than used here. The supercells within such lines tend to remain, to some degree, distinct entities (Bluestein and Weisman 2000) and have rotational dynamics that are generally well understood (e.g., Klemp 1987). However, we do attempt to clarify the structural features that distinguish the present mesovortices from the more commonly considered supercell mesocyclones. In the second part of this study (Trapp and Weisman 2003, hereafter Part II) we describe the mechanisms of low-level vortexgenesis, the role of such vortices in strong surface wind production, and their effect on QLCS structure.

We begin with a discussion of the modeling methodology used in the present study, followed by an overview of the environmental shear dependencies evident among the simulation experiments, and finish with a more specific discussion of vortex structure and evolution and the relationship to recent observational studies of such features.

2. Experimental methodology

For the experiments presented herein, the Klemp and Wilhelmson (1978) three-dimensional, nonhydrostatic, primitive equation numerical model is used. Model computations are performed in a domain 500 km in the horizontal directions and 17.5 km in the vertical direction. With this domain size and also the practice of subtracting a constant speed uniformly from the model wind profile, the QLCS remains well away from the lateral boundaries throughout its lifetime, thereby preventing potential complications due to storm–lateral boundary interactions. Horizontal gridpoint spacing is set at 1 km, with the vertical grid spacing stretched from 260 m at the lowest grid level (with the lowest grid point at 127 m) to about 700 m at the top of the domain. As recently discussed by Adlerman and Droegemeier (2002), such horizontal and vertical grid spacings are considered within the acceptable range to simulate the basic properties of low-level mesocyclones within supercell storms, which have a similar scale to the low-level mesovortices produced in the present simulated QLCSs (e.g., having typical diameters of 5–7 km and extending vertically to 3–6 km AGL). The model is integrated in time to 6 h. All simulations presented here include Coriolis forcing, which is applied only to the wind perturbations. As will be shown in Part II, the inclusion of Coriolis forcing is critical for the development of significant surface vortices.

A free-slip boundary condition is specified at the surface, which could impact the magnitude and structure of the simulated low-level wind fields. For instance, recent numerical sensitivity studies by Adlerman and Droegemeier (2002) suggest that the inclusion of surface friction can significantly impact the timing of cyclic mesocyclogenesis within supercell storms. However, the presence and strength of low-level mesocyclones did not seem to be significantly impacted. Since we are most interested in the larger time- and space scale properties of such mesovortices, we feel confident that the exclusion of surface frictional effects will not be critical to the interpretations included herein. Such effects, however, will have to be considered in future higher-resolution studies, especially those that consider the potential of such vortices to produce tornadoes.

Convection is initiated within a vertically stratified, horizontally homogeneous atmosphere using a line of five 1-K thermal perturbations, uniformly spaced 40 km apart, oriented normal to the low-level shear vector. We consider a typical warm-season environment characterized by CAPE of approximately 2200 J kg^{-1} (Fig. 3a) and a range of unidirectional wind shears for which u increases linearly from a value of zero at the ground to $U_s = 10$ m s^{-1} through 30 m s^{-1} at 2.5, 5.0, or 7.5 km AGL and then is constant throughout the rest of the troposphere (Fig. 3b). The specific shear magnitudes and depths considered in this paper are listed in Table 1.

We emphasize that our results are valid strictly for the Klemp–Wilhelmson model with parameterized Kessler-type warm-rain microphysics. Use of an ice-microphysical parameterization, for example, may result in a modified storm-generated cold pool that could result in a system evolution that proceeds slightly differently than with a warm-rain parameterization for a given environmental wind shear (e.g., Skamarock et al. 1994). While such modifications may potentially affect the specific shear magnitudes associated with transitions in system structure, the basic shear dependencies being emphasized here, however, are not found to be significantly impacted.

3. Simulation results

a. Summary of environmental shear sensitivities

The general characteristics of the simulations for the full range of environmental shears considered is sum-

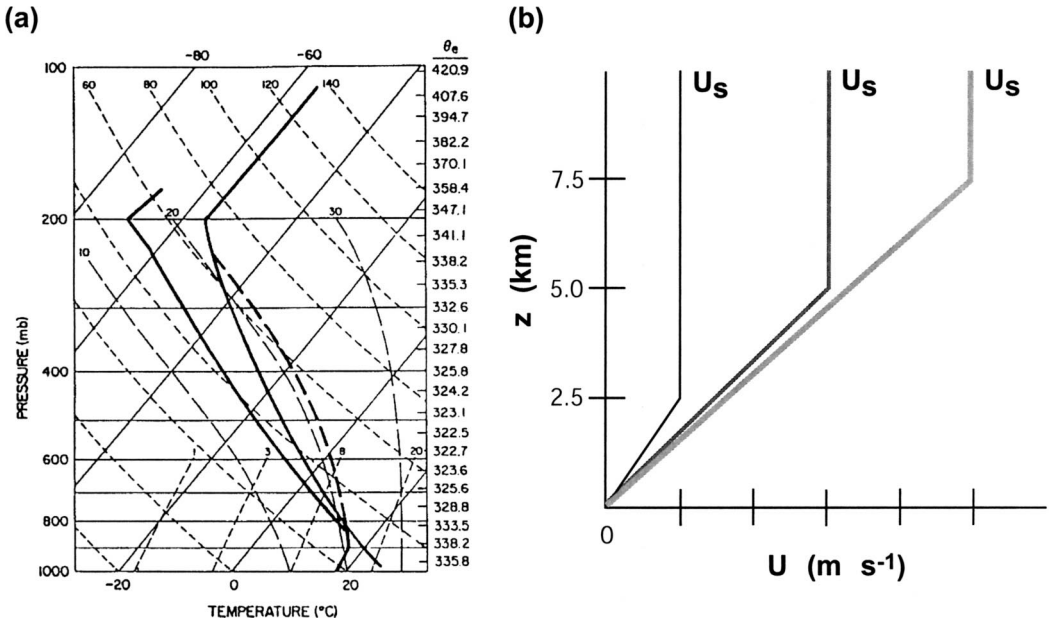

FIG. 3. (a) Thermodynamic sounding and (b) hodographs used for idealized simulations. For the hodographs, the magnitude of the shear over the prescribed depth, U_s, is varied from 10 through 30 m s^{-1}, as described in the text.

marized in Table 1, with the mature system-scale structures characterized as weak and disorganized (WK), upshear tilted (UP), organized bow echoes (BE), or supercellular (SUP), as described in the table caption. The range of moderate-shear results are further summarized in Figs. 4 and 5, which depict both low-level and midlevel structure at 4 h for the $U_s = 15$, 20, and 25 m s^{-1} 2.5 km and $U_s = 15$, 20, and 30 m s^{-1} 5 km deep-shear simulations, respectively. For the purposes of the following discussion, low level refers to 250 m AGL, while midlevel refers to 3 km AGL. As described for previous simulations (e.g., Weisman 1993; WD98), a clear trend in structure is evident for increasing magnitudes of shear, with the weaker-shear $U_s = 15$ m s^{-1} simulations characterized by scattered cells located well behind the gust front, and the stronger-shear $U_s \geq 20$ m s^{-1} simulations characterized by strong, bow-shaped segments of cells right along the leading edge of the gust front. As noted previously, lines of supercells become more prevalent as shear magnitudes increase above $U_s = 30$ m s^{-1}. The emphasis of the present study, however, is on the moderate-shear regime, for which strong, long-lived surface mesovortices associated with bowing convective segments are readily produced.

TABLE 1. Matrix of environmental shear simulations. The shear magnitude over the prescribed depth, D, is given by U_s, as described in the text. The overall organization during the QLCS's mature phase is qualitatively classified as weak, disorganized (WK), implying scattered rain cells well behind the surface gust front; upshear tilted (UP), implying a well-organized front-to-rear inflow circulation; bow echoes (BE), implying strong, bow-shaped convective lines along the leading edge of the cold pool; or supercellular (SUP), implying the existence of strong, individual cells with some supercellular characteristics scattered along the leading edge of the cold pool.

U_s (m s^{-1})	D (km)	f (10^{-4} s^{-1})	Mature mode
10	2.5	0/1	WK, UP
15	2.5	0/1	WK, UP
20	2.5	0/1/2	BE
25	2.5	0/1	BE
15	5.0	1	WK, UP
20	5.0	0/1	UP
30	5.0	0/1	BE
30	7.5	0/1	SUP, BE

All these simulated convective systems tend to evolve from an initially downshear-tilted, to upright, and then upshear-tilted configuration as the convectively generated cold pool strengthens and deepens over time (e.g., Weisman 1993). Once the system begins to tilt upshear, a rear-inflow jet is generated in response to the buoyant front-to-rear ascending current aloft and rearward-spreading cold pool at the surface (e.g., Lafore and Moncrieff 1989; Weisman 1992). For the weaker shear (e.g., $U_s = 15$ m s^{-1} over 2.5 or 5 km), this rear-inflow jet descends and spreads along the surface well behind the leading edge of the convection. For the stronger shears (e.g., $U_s \geq 20$ m s^{-1} over 2.5 or 5 km), however, this rear-inflow jet remains elevated, enhancing the lifting at the leading edge of the system and maintaining stronger and more upright convective segments along the leading edge of the system.

These shear influences on overall system structure also translate to a significant shear dependence on the structure and type of low- and midlevel vortices produced within each system. For the weaker shear $U_s = 15$ m s^{-1} over 2.5 km shear case (Figs. 4a,b), cyclonic vortices develop along the leading edge of the gust front,

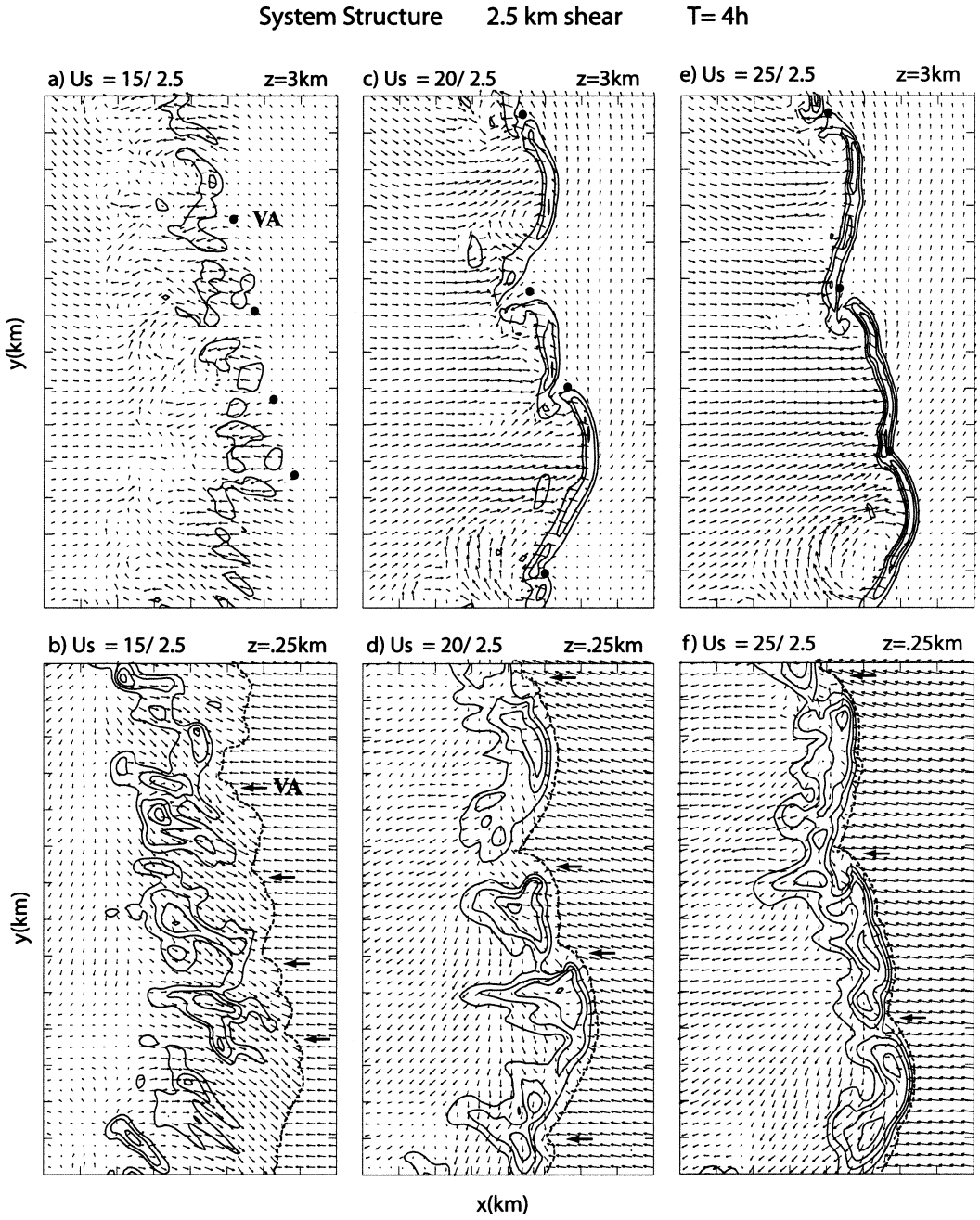

FIG. 4. Horizontal cross sections at 4 h of (a), (c), (e) system-relative flow and updraft at 3 km AGL, and (b), (d), (f) system-relative flow and rain mixing ratio at 0.25 km AGL for the U_s = 15, 20, and 25 m s^{-1} over 2.5 km shear simulations, respectively. Updraft is contoured for 4, 10, 16, and 22 m s^{-1}, and the rain mixing ratio is contoured at a 0.0015 g kg^{-1} interval. Bold arrows on the 0.25-km-AGL cross sections and bold dots on the 3-km-AGL cross sections indicate the location of significant low-level mesovortices. The dotted line depicts the cold pool (-1 K isotherm) boundary. Vectors are included every 3 km, with a vector length of 3 km equal to a wind magnitude of 18 m s^{-1}. Tick marks are included every 10 km. Only an 80 km by 140 km portion of the full domain is shown.

but, as shown in the more detailed horizontal and vertical cross sections for vortex ''VA'' (identified in Figs. 4a,b) in Fig. 6, these vortices remain very shallow (e.g., depths less than 1 km) and are not associated with updraft at midlevels. Some vortices are evident at midlevels in association with deeper convective cells well behind the leading edge of the system (not shown) but remain independent from the surface vortices. Similar surface vortices are produced for even weaker shears but are weaker in magnitude and more short-lived than those presented here.

When the shear is increased to 20 m s^{-1} over 2.5 km

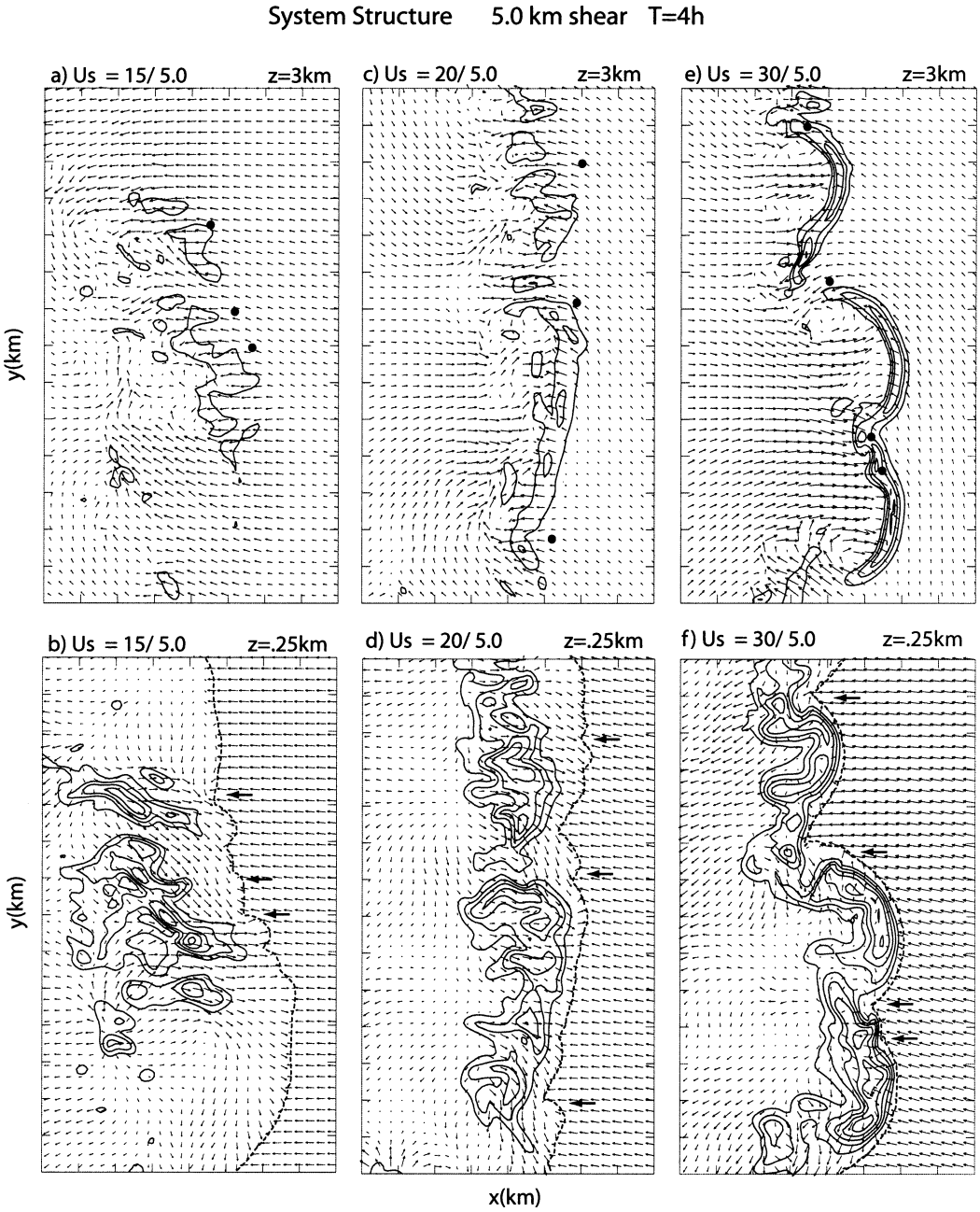

FIG. 5. Horizontal cross sections at 4 h of (a), (c), (e) system-relative flow and updraft at 3 km AGL, and (b), (d), (f) system-relative flow and rain mixing ratio at 0.25 km for the U_s = 15, 20, and 30 m s^{-1} over 5 km shear simulations, respectively, as in Fig. 4.

(Figs. 4c,d), and further to 25 m s^{-1} over 2.5 km (Figs. 4e,f), the low- and midlevel vortices are both stronger and more coherent and are now tied mostly to the ends of bow-shaped updraft segments along the leading edge of the system. There is also now a clearer connection between the low- and midlevel cyclonic vortices than for the weaker-shear cases, although the vortices still tilt rearward and now also southward, with height over the cold pool. As in the weaker-shear cases, the low-level vortices are located on the cool side of the gust front and within a region of converging flow (shown later). The midlevel vortices are generally located behind the primary updraft, as previously described for midlevel book-end or line-end vortices (e.g., Weisman 1993; WD98). Unlike in the weaker-shear case, the low-level vortices are now located beneath a midlevel updraft and, thus, are potentially subject to deeper vertical stretching. Anticyclonic vortices are also now evident

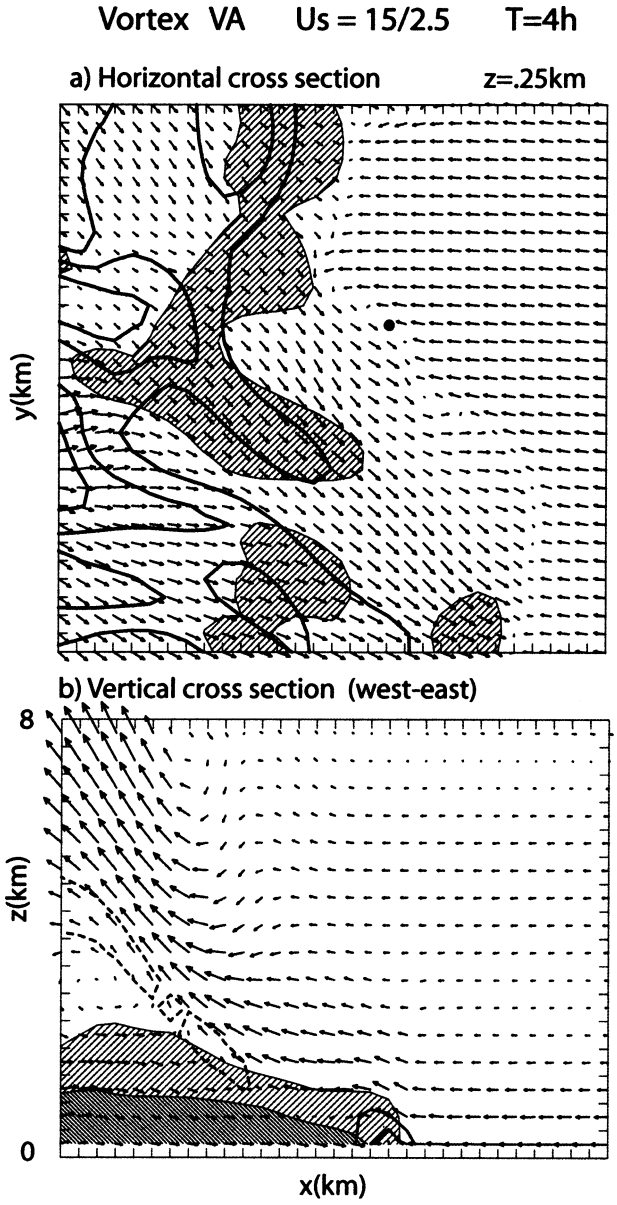

FIG. 6. (a) Horizontal cross sections at 0.25 km AGL of system-relative flow, rain mixing ratio, and 3-km-AGL updraft, and (b) vertical cross sections of system-relative flow and vertical vorticity for vortex VA from the $U_s = 15$ m s^{-1} over 2.5 km shear simulation at 4 h. In (a), updraft is lightly hatched for magnitudes between 4 and 12 m s^{-1} and darkly hatched for magnitudes greater than 12 m s^{-1}. Rain mixing ratio is contoured using a 0.0015 g kg^{-1} interval. Bold dot indicates the location of vertical cross sections shown in (b). In (b), vorticity is contoured using a 40×10^{-4} s^{-1} interval. Vectors are included every grid point, with a vector length of one grid point equal to a wind magnitude of 20 m s^{-1}. Tick marks are included every kilometer. In (a), only a 30 km by 30 km portion of the full domain is shown. In (b), only an 8-km portion of the full vertical domain is shown.

at 3 km, behind the southern ends of bow-shaped segments, as also discussed by Weisman (1993) and WD98, but no companion anticyclonic vortices exist at low levels (an explanation for which is offered in Part II).

A similar dependence on shear is also noted for the 5-km deep-shear simulations (Fig. 5). For $U_s = 15$ m s^{-1} over 5 km (Figs. 5a,b), low-level vortices are produced, but they again remain shallow (e.g., depths less than 1 km) as the updraft current tilts rapidly rearward, with rain cells scattered well behind the leading edge of the cold pool. As U_s increases to 20 m s^{-1} over 5 km (Figs. 5c,d), the leading edge convection becomes relatively stronger and more upright, as do the mesovortices, with both cyclonic and anticyclonic line-end vortices now evident at midlevels. However, these features are still less pronounced/weaker than those in the case when $U_s = 20$ m s^{-1} is confined to just 2.5 km (e.g., Figs. 4c,d). Increasing the shear to $U_s = 30$ m s^{-1} over 5 km (Figs. 5e,f) again produces strong, upright, bow-shaped segments along the leading edge of the system, with a strong rear-inflow jet and midlevel line-end vortices, as also noted for the stronger, shallower-shear cases. Strong, low-level cyclonic vortices are again found in association with the cyclonic midlevel line-end vortices, but some very significant low-level vortices are now also found along and just north of the apex of some of the interior bowing segments (e.g., Fig. 5f). As will be shown in the next section, such vortices tend to increase in size and depth over time, subsequently moving northward, relative to the bowing segment, and replacing the preexisting line-end vortex structure. Also more evident in these stronger-shear cases is hooking or notching in the low-level rainwater field, reminiscent of structures associated with high-precipitation-type supercells (Moller et al. 1994). Although supercell-type structures can be produced in simulated lines given deeper, stronger environmental shear (e.g., Bluestein and Weisman 2000), the hook structures in the present cases, which reflect the rotational character of the low- and midlevel flow, are not associated with long-lived, midlevel rotating updrafts, as with supercell storms. We should also note that a magnitude of vertical wind shear of $U_s = 30$ m s^{-1} over 5 km is sufficient to produce long-lived, splitting supercells (as opposed to bow echoes) when convection is triggered as an isolated cell rather than a line of cells (e.g., Weisman and Klemp 1982, 1984), emphasizing the importance of cell interactions in controlling the predominant convective mode in certain cases.

Thus, although some degree of low-level vortex formation is evident for all of the environmental shears considered, the vortices become especially significant in terms of strength and depth for shear magnitudes of 20 m s^{-1} or greater over the lowest 2.5–5 km AGL. This shear regime also seems reasonably consistent with the environments identified observationally as especially conducive to the production of significant vortices and tornadoes within such quasi-linear convective sys-

tems (e.g., Funk et al. 1999; DeWald and Funk 2000). Based on this, we will focus the remaining discussion on these stronger-shear simulations. In particular, we will look in more detail at the evolution of vortices for the $U_s = 20$ m s^{-1} over 2.5 km and the $U_s = 30$ m s^{-1} over 5 km simulations.

b. The $U_s = 20$ m s^{-1} over 2.5 km shear simulation

The more detailed evolution of the $U_s = 20$ m s^{-1} over 2.5 km shear simulation is now presented in Fig. 7 at 1-h intervals, with the ground-relative tracks of the more significant low-level vortices, as labeled in Fig. 7, presented in Fig. 8. Over the first 2 h, an initial line of cells matures and decays (not shown), and, by 2 h, a new sequence of cell clusters has matured along a consolidating gust front (Figs. 7a,b). The spacing of these cell clusters is still reflective of the spacing of the initial bubbles, with the new cells having developed at the collision point between the outflows of the original cells. At midlevels (Fig. 7a), the updrafts have begun to develop into more continuous 30-km segments along the leading edge of these cell clusters, with cyclonic and anticyclonic book-end vortices becoming evident behind the northern and southern ends of each segment, respectively, as described by Weisman (1993). Localized rear-inflow jets have begun to develop between the book-end vortices, impinging at the apex of each updraft segment. At low levels (Fig. 7b), four cyclonic vortices (V0, V1, V2, V3) can be identified at the leading edge of the convective segments, with some associated notching also evident in the low-level rain field.

By 3 h (Figs. 7c,d), these cell clusters and updraft segments have begun to merge into a continuous line of bowing segments of various lengths. At midlevels, cyclonic and anticyclonic book-end vortices are still evident at the ends of individual segments, but the pattern is becoming quite a bit more complicated as some of the segments have grown in scale and are interacting with neighboring segments. A more general rear-inflow current has begun to develop behind the entire convective line at midlevels, with more concentrated rear-inflow jets still evident behind some of the more organized bowing segment. At low levels, vortices V1 and V2 have grown somewhat in size while moving closer together, and a new vortex, V4, located at the northen end of one of the more continuous reflectivity segments, has now developed out of the decaying V0. In the meantime, V3 has propagated out the north boundary of the presented domain. While initially located independent of the midlevel vortices, both V1 and V4 are now located just to the north of the northern cyclonic book-end vortices associated with their respective bowing segments.

Between 3 and 4 h, the convection consolidates into three primary bow segments, with V4 remaining at the northern end of the expanding southernmost bow, and V1 and V2 now merging to create vortex V5 at the northern end of a small middle bow (e.g., Fig. 8). As at 3 h, both low-level vortices are located to the north of the cyclonic midlevel vortices (Figs. 7e,f). Although anticyclonic book-end vortices are still evident at 3 km behind the southern ends of some of the bow segments, no significant anticyclonic vortices develop at low levels. This consolidation process continues after 4 h, and by 6 h (Figs. 7i,j), only two large bow segments are evident within the presented domain, with cyclonic and anticyclonic book-end vortices aloft, and cyclonic shear and vortices evident at low levels, extending from the apex of each bow northward to a primary vortex at the northern end.

At 5 h (Figs. 7g,h), a new low-level vortex, V6, develops within the cyclonic shear zone that extends south of V4, and subsequently merges with V4 to create V7 by 6 h (e.g., Fig. 8). The development of a new vortex within a cyclonic shear zone extending south of an existing vortex, and then its merger with that vortex, is a common characteristic of the mature stage of our simulated bow echoes, as will also be shown for the stronger-shear simulation to follow. Such merging, or ''upscale growth,'' is also identified in radar observations (e.g., Przybylinski 1995) and resembles the merging process of isolated coherent vortices in two-dimensional turbulent flows (e.g., McWilliams 1984) or of misocyclone-scale vortices in nonsupercellular convective lines (Lee and Wilhelmson 1997). Whether the upscale growth of the mesovortices in our simulated QLCSs is inherently two-dimensional or somehow related to the three-dimensional evolution of the convective system is left for further study.

As shown in Fig. 8, all of the low-level vortices described above attain a magnitude of at least 10^{-2} s^{-1} during their lifetime, which can exceed 2 h. Also, while the cyclonic vortices propagate slightly southward at early times, or to the right of the mean wind and wind shear, slight northward and southward propagation are both evident after this time, consistent with the tendency for the vortices to merge. After 4 h, the propagation of the more consolidated vortices is predominantly west to east, with little deviate motion relative to the mean wind or wind shear evident. It should be noted that this lack of consistent or significant deviate motion is in contrast to the deviate motion of mesocyclones associated with supercell storms, which propagate significantly to the right of the mean wind or wind shear.

Figures 9 and 10 present a more detailed evolution of one of the earlier low-level vortices, V0. This vortex first becomes apparent at about 1 h 40 min as an elongated vorticity maximum just behind the leading edge of the gust front, on the cyclonic-shear side of a maximum in northwesterly low-level outflow from of a decaying rain cell (Fig. 9a). Note that at this time, the vorticity maximum actually occurs as part of a couplet that is symmetric about this rain cell (see also Part II). Although located in a region of strong low-level convergence, the incipient vortex is about 4 km ahead of main updraft region aloft. Some cyclonic shear and cur-

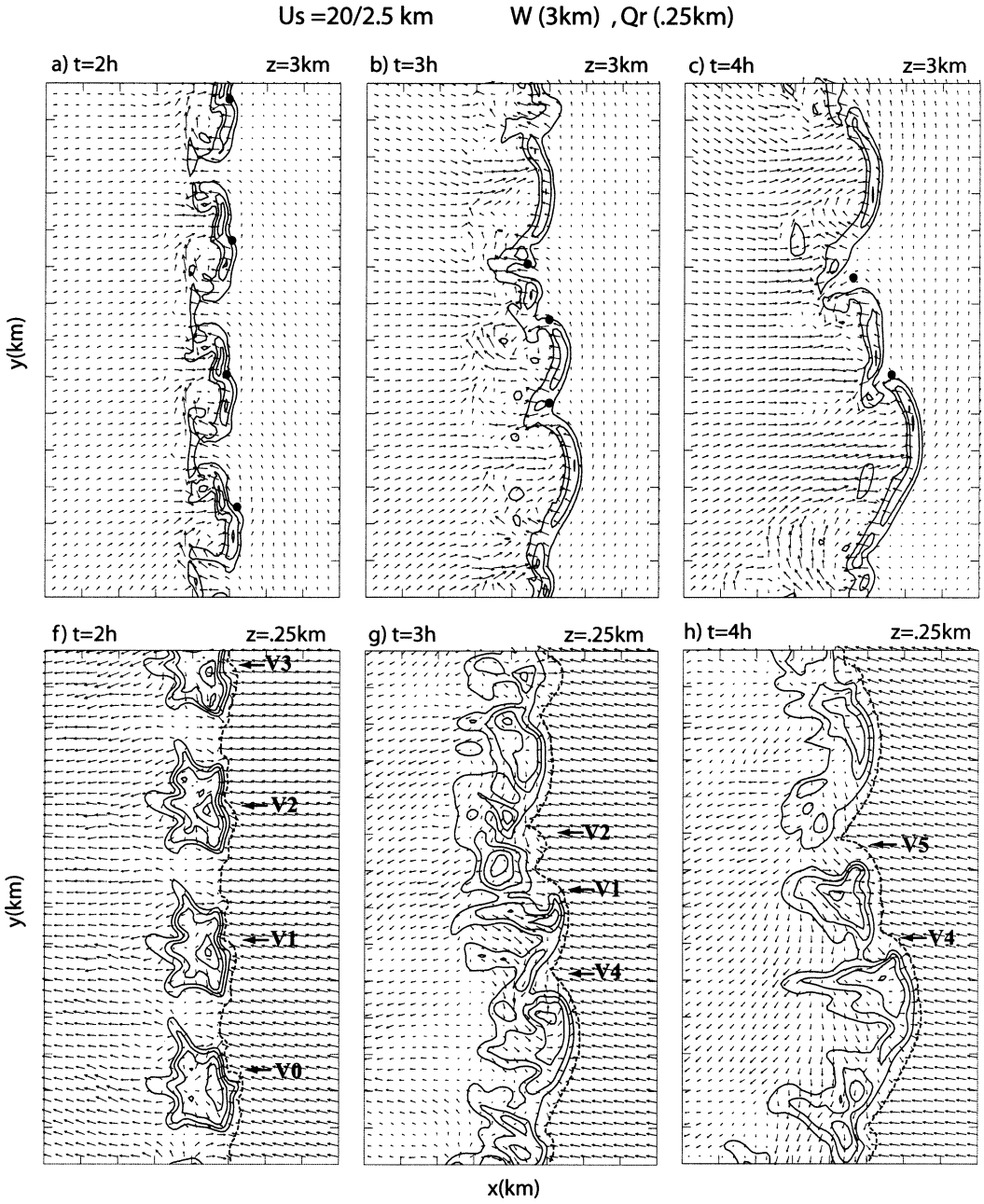

FIG. 7. Horizontal cross sections at hourly intervals, starting at 2 h, of (a), (b), (c), (d), (e) system-relative flow and updraft at 3 km AGL, and (f), (g), (h), (i), (j) system-relative flow and rain mixing ratio at 0.25 km AGL for the $U_s = 20$ m s^{-1} over 2.5 km shear simulation, respectively, as in Fig. 4. Bold arrows on the 0.25 km AGL cross sections and bold dots on the 3 km AGL cross sections indicate the location of significant low-level mesovortices, which are additionally labeled V1, V2, V3, etc., as described in the text.

vature is also evident at 3 km in association with the updraft regions, but no distinct vortices are apparent at this level at this time (Fig. 10a).

By 2 h (Figs. 9b, 10b), the decaying rain cell has been replaced by a single, strong cell with an associated divergent low-level outflow. The low-level vortex has become much better organized at this time and is located just north of the maximum of this outflow. This is also the location of a forward appendage in the rain field, somewhat reminiscent of a spearhead echo, as originally described by Fujita (1978). The low-level vortex is also now located beneath a significant updraft aloft, enhancing the probability of further strengthening via vortex stretching. A small, weak vortex is also now evident at 3 km AGL to the southwest of the low-level vortex, associated with a break in an otherwise continuous mid-

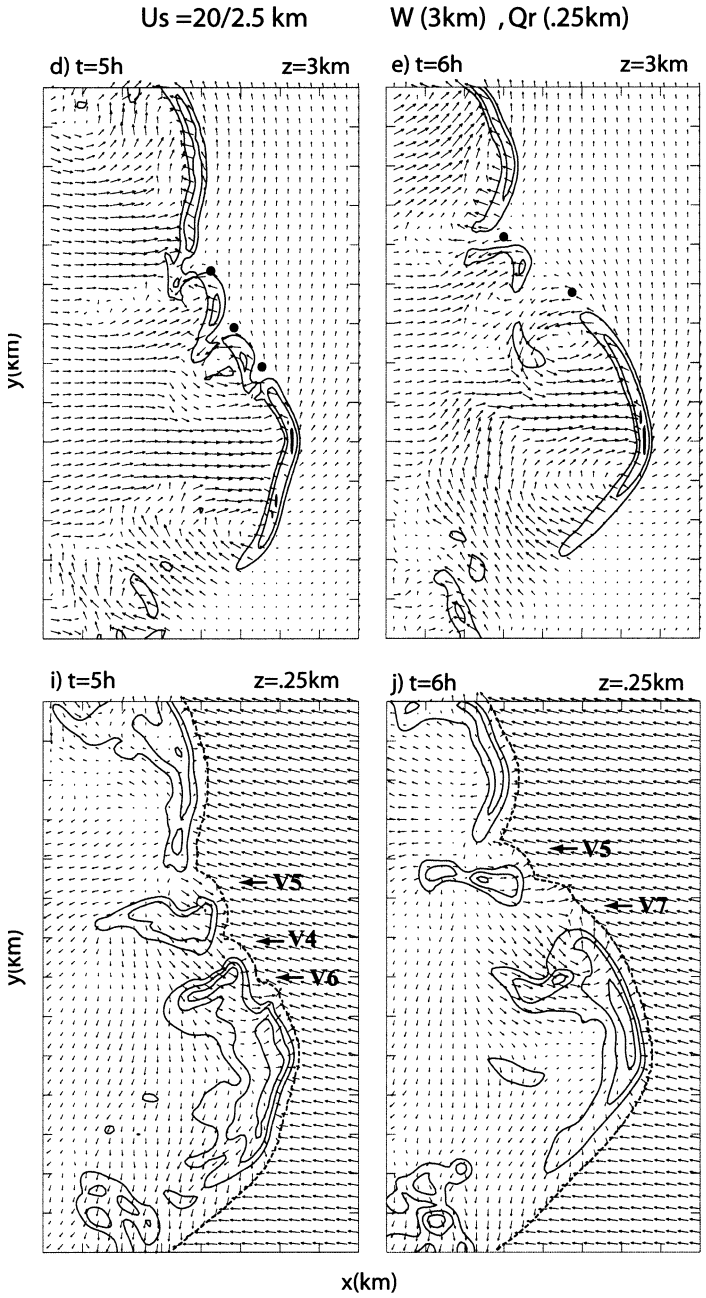

FIG. 7. (*Continued*)

level updraft. The most significant vortices at 3 km at this time, however, are the northern cyclonic and southern anticyclonic book-end vortex pair that have developed at the ends of this convective segment but are not associated with comparable vortices near the surface.

By 2 h 20 min (Figs. 9c, 10c), the midlevel updraft segment previously north of the low-level vortex has dissipated, while the southern half has maintained its strength. The low-level vortex is now located north of this updraft segment, and appears more diffuse than earlier. The associated cyclonic midlevel vortex, however, has grown in scale, and now resides behind the northern end of the updraft segment, taking on characteristics similar to the previous northern book-end vortex. Both the low- and midlevel vortices continue to grow in scale over the next 20 min (Figs. 9d, 10d) while maintaining a similar structural relationship with the northern end of the convective segment. As shown in Fig. 7, this vortex system is traceable through 5 h, after which it merges with a similar vortex system to the north.

Figure 11 presents vertical cross sections through the

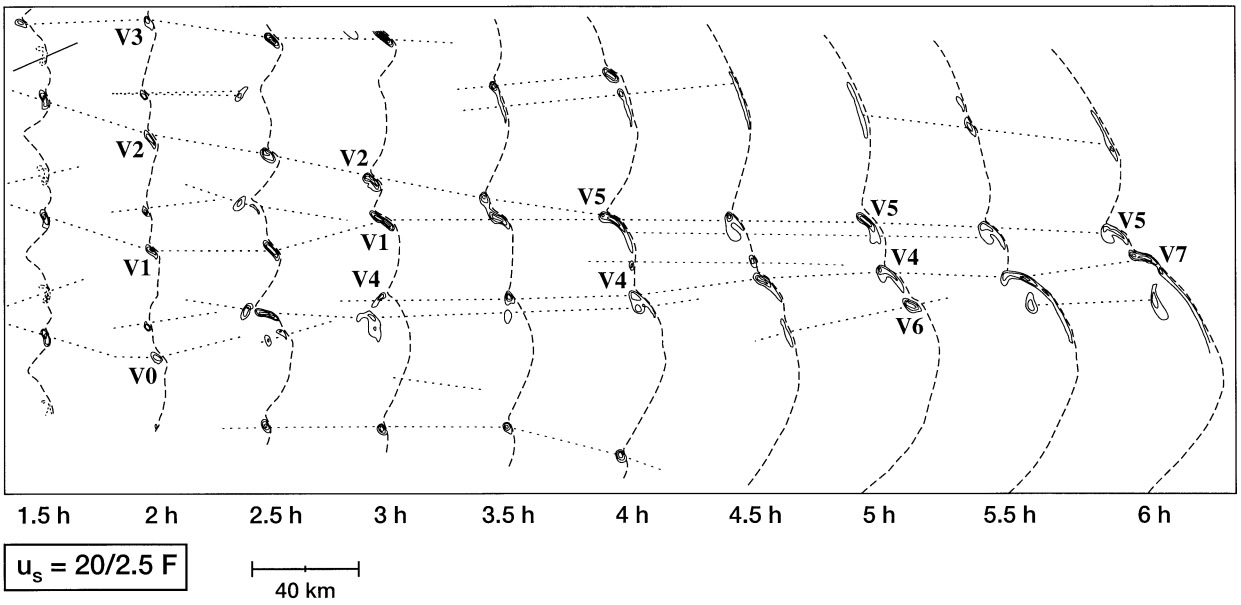

FIG. 8. Ground-relative tracks of significant low-level mesovortices for the $U_s = 20$ m s^{-1} over 2.5 km shear simulation, as also identified in Fig. 7. Positive vertical vorticity is contoured using a 50×10^{-4} s^{-1} interval, with the zero contour omitted. The thick dashed line denotes the location of the surface cold pool boundary.

core of V0 at 20-min intervals during its developing stages. Since the nearest midlevel vortex resides to the southwest of the low-level vortex, these cross sections are taken from northeast through southwest (45°) through the low-level vortex, as shown in Fig. 9. At 1 h 40 min (Fig. 11a), the low-level shear vorticity is quite shallow and separate from a region of midlevel vorticity, with both regions of vorticity residing in weak updraft. By 2 h (Fig. 11b), the earlier midlevel region of vorticity has dissipated, but the low-level vortex has strengthened to greater than 10^{-2} s^{-1} and deepened significantly to 4 km AGL, in respone to an intensifying and deepening leading edge updraft. In addition, a significant rear-inflow jet is now beginning to impinge into the updraft and vortex region. However, the vortex subsequently becomes shallower and weaker, as the updraft tilts more and more rearward over time (Figs. 11c,d).

c. The $U_s = 30$ m s^{-1} over 5 km shear simulation

A more detailed evolution for the $U_s = 30$ m s^{-1} over 5 km deep-shear case is presented in Fig. 12, with the ground-relative tracks of the more significant low-level vortices presented in Fig. 13. This magnitude of shear is sufficient to produce initial cell splitting (some weak splitting was also noted for the $U_s = 20$ m s^{-1} over 2.5 km simulations), but by 2 h (Figs. 12a,b), the original split cells have dissipated, with new updrafts now developing along the leading edge of four separate cell clusters. Four significant low-level vortices are identified within the domain at this time, three of which (Va, Vb, Vd) are located at the northern end of strong rain cells, and a fourth (Vc) associated with a weaker rain cell. A more complicated collection of both cyclonic and anticyclonic vortices is noted at 3 km AGL.

These cell clusters again evolve into well-formed bowing segments by 3 h (Figs. 12c,d), with cyclonic and anticyclonic book-end vortices evident at midlevels and significant cyclonic vortices still being found at low levels. Vortices Va and Vd maintain their identity during this time period, while vortices Vb and Vc merge to create Ve (e.g., Fig. 13). Additionally, a new vortex, Vf, has developed near the apex of the bow segment between Va and Ve. A weak system-scale rear-inflow jet is just beginning to develop at 3 km AGL, with stronger, more localized rear-inflow jets also evident just behind each bowing segment.

The bow segments continue to strengthen and expand after 3 h, with the two southernmost bows merging into one bow by 6 h (Figs. 12i,j), with one set of book-end vortices and an associated strong rear-inflow jet at 3 km AGL now encompassing this combined larger bow. Vortex Vd maintains its identity throughout this time period (Fig. 12f), while a more complicated pattern of merger and redevelopment is noted for the remaining low-level vortices. For example, vortices Vh and Vi, which (re) develop out of a decaying Va, subsequently merge into Vj by 5 h (Fig. 13).

Strong near-surface winds are produced all along this convective system throughout most of its lifetime. However, the most intense winds are often associated with the most significant low-level vortices, which are located near the northern end of each bow segment. This is especially evident at 6 h (Fig. 12j), where an exceptionally large area of strong winds (35–45 m s^{-1} in a ground-relative reference frame) is produced in asso-

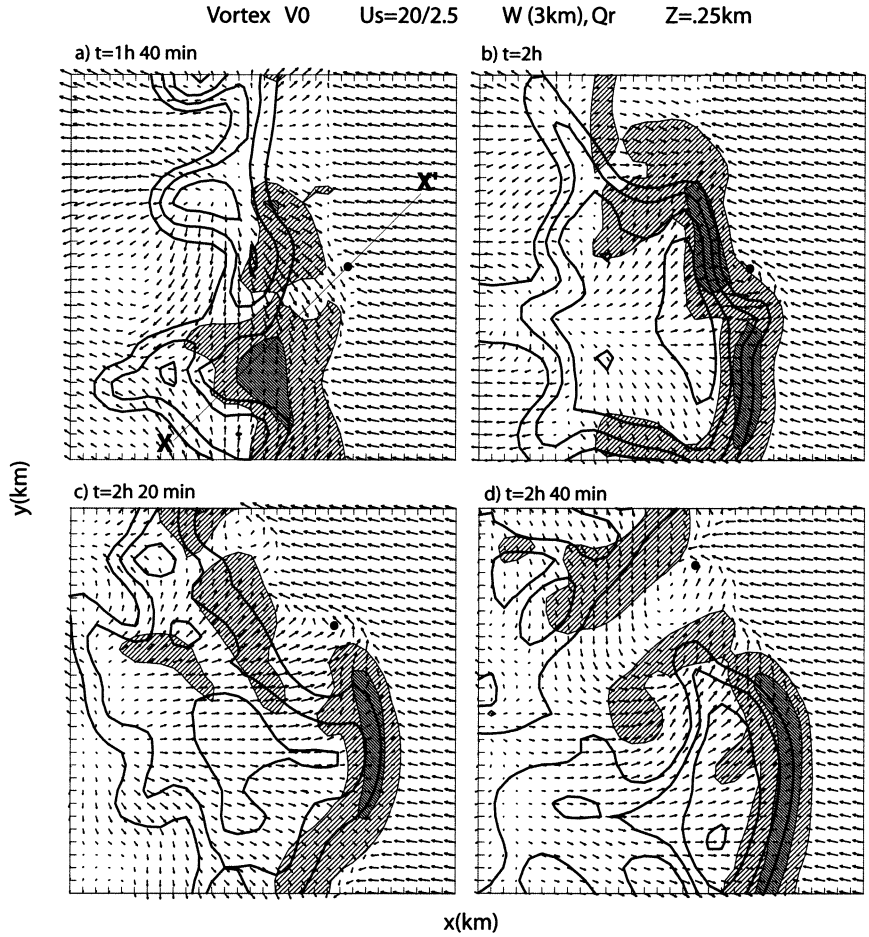

FIG. 9. Horizontal cross sections at 0.25 km AGL of system-relative flow and rain mixing ratio and at 3 km AGL for updraft at (a) 1 h 40 min, (b) 2 h, (c) 2 h 20 min, and (d) 2 h 40 min for vortex V0 for the $U_s = 20$ m s^{-1} over 2.5 km shear simulation. Updraft is lightly hatched for magnitudes between 4 and 12 m s^{-1} and darkly hatched for magnitudes greater than 12 m s^{-1}. Rain mixing ratio is contoured using a 0.0015 g kg^{-1} interval. Bold dots indicate the location of vertical cross sections shown in Fig. 11. Vectors are included every grid point, with a vector length of one grid point equal to a wind magnitude of 20 m s^{-1}. Tick marks are included every kilometer. Only a 30 km by 30 km portion of the full domain is shown.

ciation with the merging low-level vortices Vg, Vj, and Vk. A similar area of enhanced near-surface winds associated with a low-level vortex at the northern end of a bow segment is also evident for the $U_s = 20$ m s^{-1} shear case at 6 h (Fig. 7j). A more complete analysis and discussion of damaging near-surface winds associated with such mesovortices is provided in Part II.

As with the $U_s = 20$ m s^{-1} over 2.5 km simulation, the low-level vortices are again quite long-lived as they propagate predominantly west to east along with the individual bowing segments (Fig. 13). Three primary vortex groupings can be identified, associated with each of the three primary bowing segments noted above. Other more isolated vortex centers are found within vorticity-rich regions that extend from the apex of each bow segment northward (Fig. 13). Many of these embedded vortices develop along the leading edge of the bow and then propagate northward relative to the bow segment, grow upscale, and eventually become engulfed by, or define, a new book-end vortex structure.

A more detailed evolution of a characteristic north-of-apex vortex is presented in Figs. 14 and 15 for the vortices Vh and Vi. At 3 h 40 min, vortex Vh, which developed within the cusp between the middle and southern bow segments, is already well established, extending from near the surface through 3 km AGL (Figs. 14a, 15a). A region of cyclonic shear extends south from this vortex, along a continuous bow-shaped region of precipitation and updraft, but no other significant vortices are evident at this time. Twenty minutes later (Figs. 14b, 15b), Vh is associated with a well-formed hook in the rain field. However, vortex Vi is now developing 10 km farther south, associated with a new notching in the previously continuous rain field. At low levels, Vi is about 4–5 km in diameter and is located just behind the leading edge of the gust front, but still underneath strong

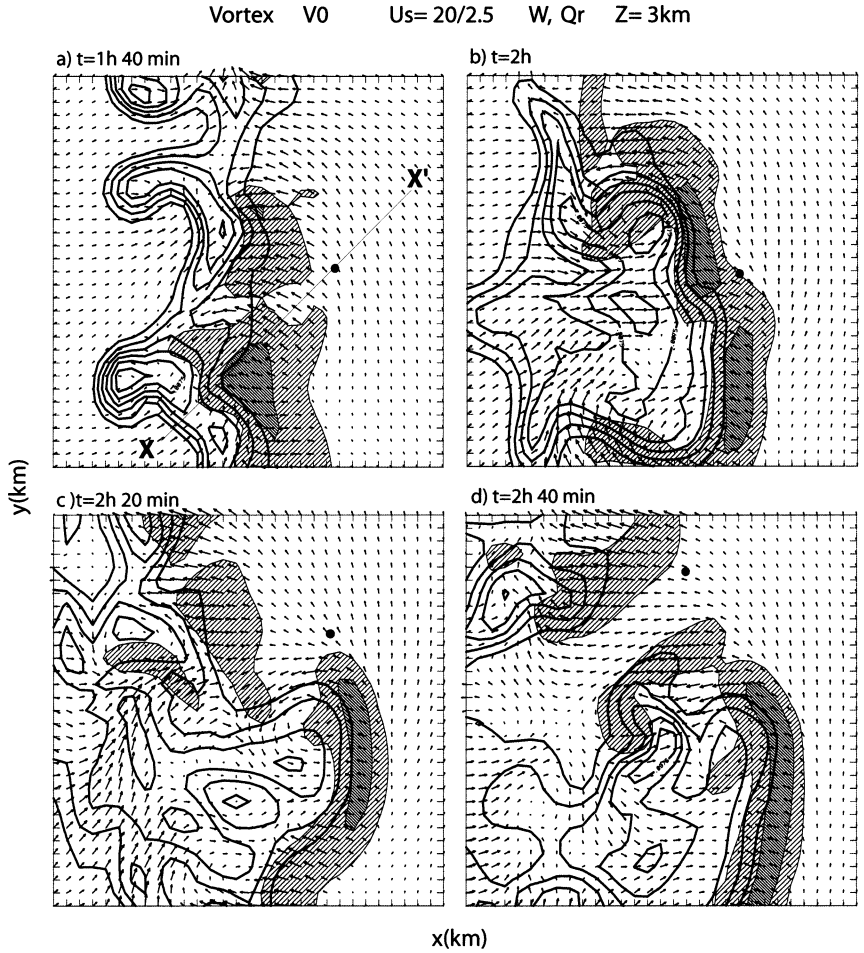

FIG. 10. Horizontal cross sections at 3 km AGL of system-relative flow, updraft, and rain mixing ratio at (a) 1 h 40 min, (b) 2 h, (c) 2 h 20 min, and (d) 2 h 40 min for vortex V0 for the $U_s = 20$ m s^{-1} over 2.5 km shear simulation, as described for Fig. 9.

updraft at 3 km AGL. The vortex tilts rearward with height and, at 3 km, is located on the back edge of the updraft region.

By 4 h 20 min (Figs. 14c, 15c), Vh has weakened significantly, while Vi continues to strengthen and is now associated with a well-formed hook in the rain field. The low-level vortex is still located beneath a strong updraft aloft but, at 3 km, is now associated with a downdraft at its core, surrounded by a weak updraft. Vortex, Vi continues to grow in scale and, by 4 h 40 min (Figs. 14d, 15d), has forced a fracture of the updraft region (see Part II), with the low-level vortex now located under the weak updraft aloft and the midlevel vortex located in a weak updraft and even downdraft. This vortex configuration is maintained through 5 h (e.g., Figs. 12i,j) while continuing to grow in scale, with the region of significant circulation now extending 10–12 km across.

Figure 16 presents vertical cross sections of vertical vorticity through vortex Vi at 20-min intervals during its early-through-mature phase. The cross sections are taken at 45° through the vortex, as shown at 4 h in Fig. 14. At 3 h 40 min (Fig. 16a), there is little evidence of a low-level vortex, but weak vorticity is evident extending through the midlevels, located on the back edge of the main updraft region. By 4 h (Fig. 16b), a low-level vortex has now strengthened to over 2×10^{-2} s^{-1} within the region of strong surface convergence and updraft. The vortex strengthens to over 3×10^{-2} s^{-1} by 4 h 20 min (Fig. 16c), with a magnitude of greater than 2×10^{-2} s^{-1} now extending up through 5 km AGL. Although the vortex is clearly associated with updraft on its forward side, the correlation between the updraft and vertical vorticity is quite weak (e.g., a linear correlation coefficient of only 0.1–0.2 over the depth of the vortex; not shown). This point is revisited in section 4, when the present vortices are compared to mesocyclones within supercell storms. The vortex weakens somewhat after this time, as the updraft migrates further to its leading edge, and, by 4 h 40 min (Fig. 16d), the core of the vortex is now actually located within a downdraft. Thus, unlike the line-end vortices described by

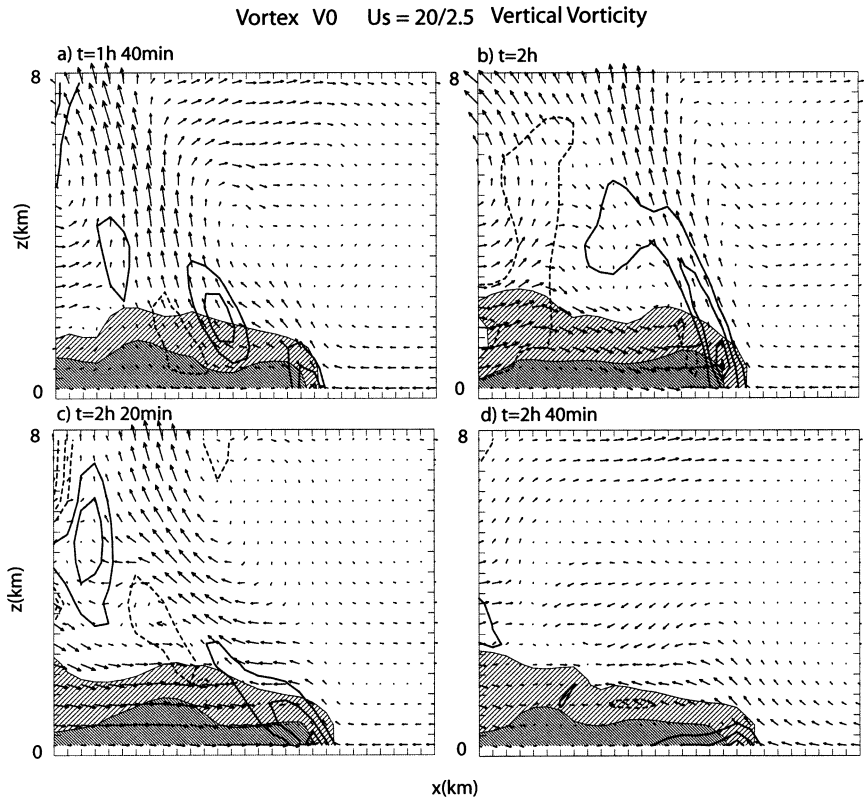

FIG. 11. Vertical cross sections of system-relative flow and vertical vorticity at (a) 1 h 40 min, (b) 2 h, (c) 2 h 20 min, and (d) 2 h 40 min, taken at a 45° angle through the low-level mesovortex, as indicated by the bold dots in Fig. 9, for vortex V0 for the $U_s = 20$ m s^{-1} over 2.5 km shear simulation. Vorticity is contoured using a 40×10^{-4} s^{-1} interval. The θ' field is shaded for -1 to -4 K (light hatching) and less than -4 K (dark hatching). Vectors are shown at every grid point in the horizontal and vertical, with a horizontal vector length of one grid point equal to a vector magnitude of 15 m s^{-1}. Only an 8-km portion of the full vertical domain is shown.

Weisman (1993) and WD98, which developed at midlevels independent of near-surface vortices, the present low-level vortex builds upward over time to become a line-end-type vortex.

d. Summary

The low-level mesovortices produced for both the $U_s = 20$ m s^{-1} over 2.5 km AGL and the $U_s = 30$ m s^{-1} over 5 km AGL simulations have much in common, including their basic structure, longevity, propagation, and merging tendencies and their north-of-apex preference with respect to each bowing segment. However, some systematic differences are evident as the strength and depth of the environmental shear increases, including a stronger, deeper, and more upright vortex orientation and a closer correspondence between the low-level mesovortices and the cyclonic midlevel book-end vortices located behind the northern ends of the bow segments. These differences are directly related to the overall impact of environmental shear on system structure, as also discussed earlier, in that stronger environmental shear, especially at lower levels, also results in a more upright convective orientation, with stronger and deeper leading-edge updrafts. These differences may have implications for severe weather production, especially for the potential generation of tornadoes within such mesovortices, which require strong, deep stretching by an associated updraft.

4. Comparison to supercell mesocyclones

The strength and size of the low- and midlevel vortices produced in the above idealized simulations are quite comparable to that of mesocyclones associated with supercell storms. The additional collocation of some of these vortices with hook structures in the rain field (e.g., Fig. 14d) might lead one to believe that these features are associated with supercells embedded within the more linear, larger-scale convective system. Indeed, the existence of embedded supercells has been used to explain damaging winds within observed quasi-linear systems (e.g., Miller and Johns 2000). Supercell-type structures are produced in the present simulations at early times for magnitudes of U_s greater than 20 m s^{-1}, when the cells composing the convective system are

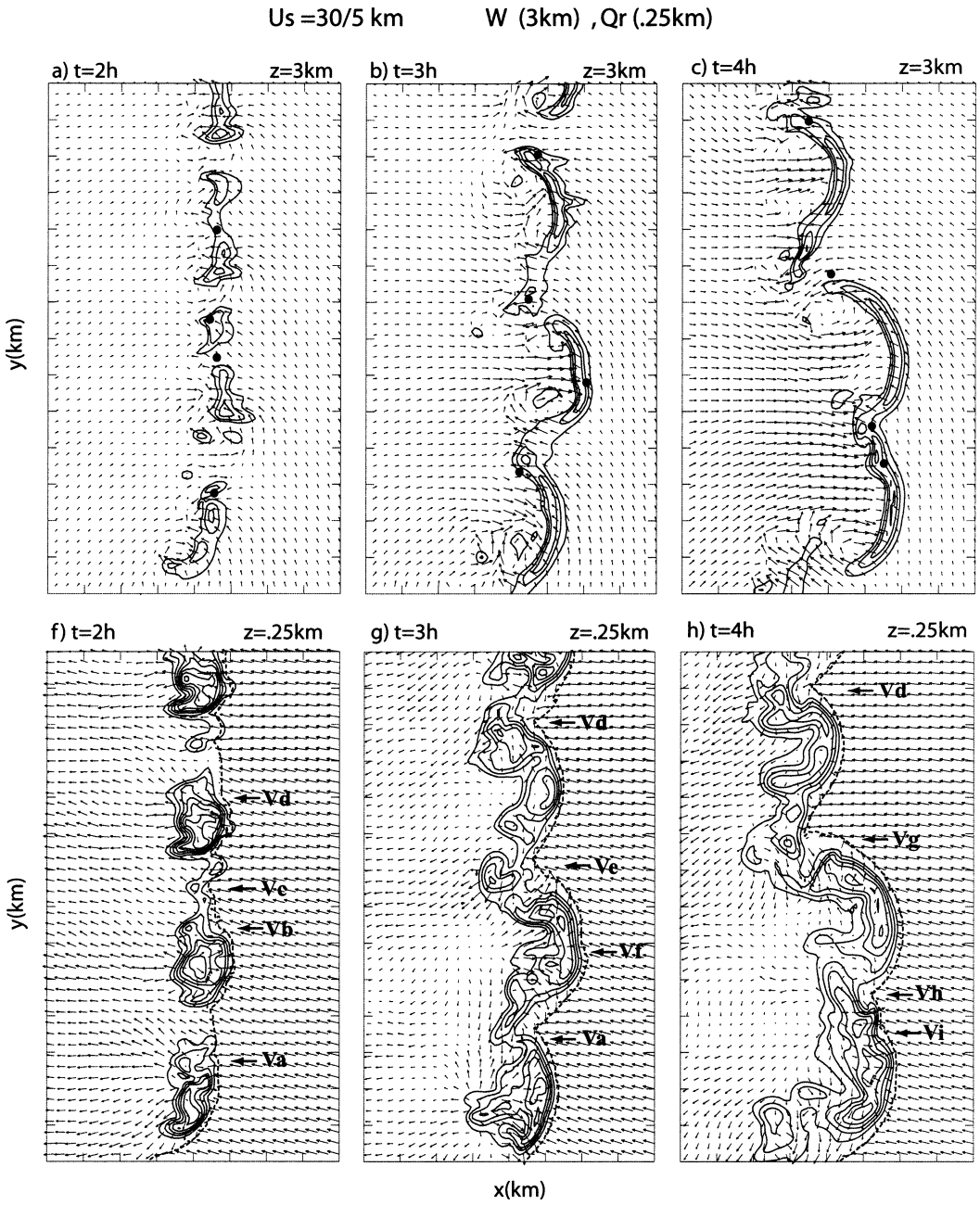

FIG. 12. Horizontal cross sections at hourly intervals, starting at 2 h, of (a), (b), (c), (d), (e) system-relative flow and updraft at 3 km AGL and (f), (g), (h), (i), (j) system-relative flow and rain mixing ratio at 0.25 km AGL for the $U_s = 30$ m s^{-1} over 5 km shear simulation, respectively, as in Fig. 4.

more isolated; supercells are even more prevalent in simulations of convective lines with even stronger and deeper shears than presented here (e.g., Weisman et al. 1988; Bluestein and Weisman 2000). However, we must reiterate that the vortices described in the above analyses are not associated with embedded supercells and, indeed, have structural features quite distinct from supercell mesocyclones.

In order to more clearly illustrate the structural differences between mesocyclones associated with supercell storms and mesovortices produced in the present simulations, we include herein an additional simulation of an isolated supercell using the same thermodynamic profile and grid spacing as for the above simulations, but now using a vertical shear profile more typical of supercell environments (e.g., with $U_s = 35$ m s^{-1} over the lowest 6 km AGL, with the shear vector turning clockwise over the lowest 2 km AGL) (Fig. 17). With

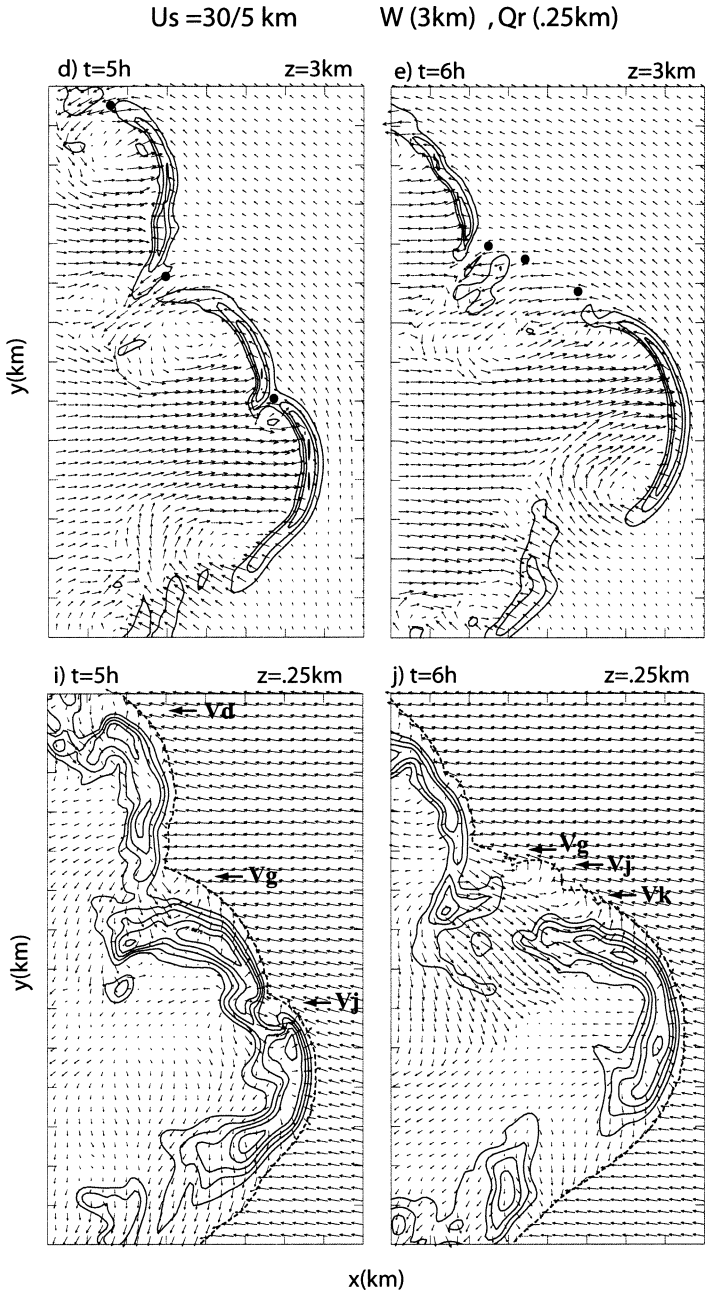

FIG. 12. (*Continued*)

the exception of the use of a vertically stretched grid for the present simulation, this simulation is identical to one discussed in Weisman and Rotunno (2000) and produces an archetypical supercell storm with a strong, rotating midlevel updraft and an associated surface mesocyclone.

The mature storm structure is presented in Fig. 18, which depicts horizontal cross sections of storm-relative flow, updraft, and rainwater at 90 min at 0.25 and 3 km AGL, as for the above simulations, and also at 6 km AGL, to emphasize the deeper character of the supercell mesocyclone. Most noteworthy is the strong, rotating updraft and associated hook feature in the rain field extending through midlevels of the storm, with a low-level mesocyclone centered directly beneath the updraft aloft. A vertical cross section taken east–west through the storm (Fig. 19b) clearly depicts a strong midlevel mesocyclone extending through 8 km AGL that is well correlated with the midlevel updraft, and a relatively distinct mesocyclone beneath, near the surface that is also located within the low-level updraft. The linear correlation coefficient calculated for the updraft region

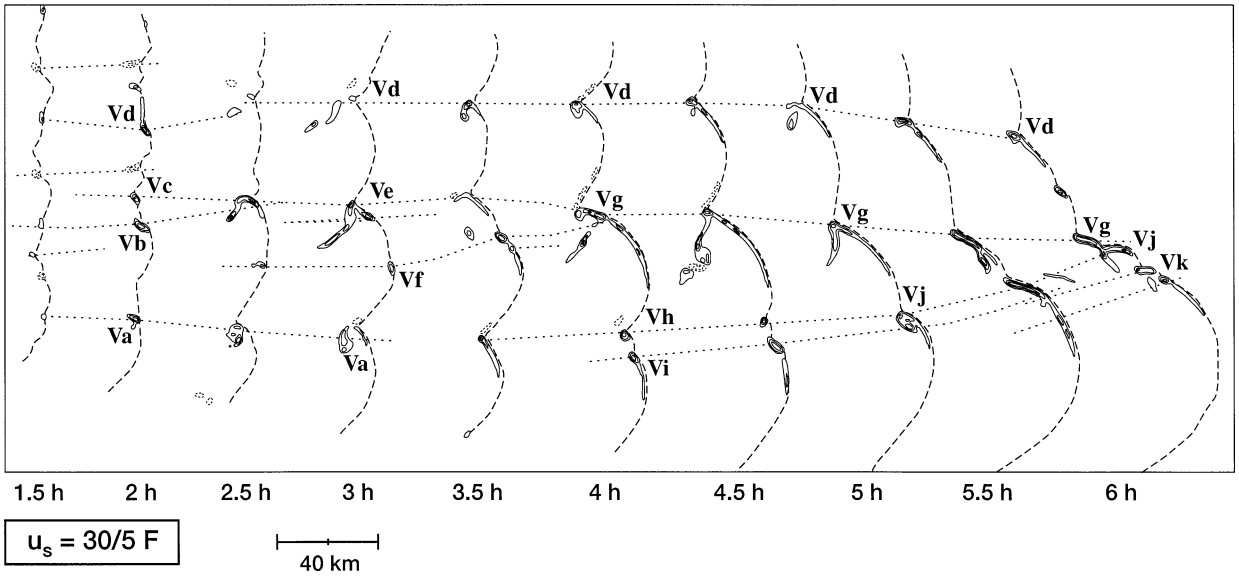

FIG. 13. Ground-relative tracks of significant low-level mesovortices for the $U_s = 30$ m s^{-1} over 5 km shear simulation, as also identified in Fig. 12. Positive vertical vorticity is contoured using a 50×10^{-4} s^{-1} interval, with the zero contour omitted. The thick dashed line denotes the location of the surface cold pool boundary.

surrounding this mesocyclone averaged between 0.5 and 0.6 over the depth of the mesocyclone (not shown), in stark contrast to the much lower linear correlations of 0.1–0.2 noted for the bow-echo mesovortex described in section 3c.

An important characteristic of supercell storms is that such midlevel mesocyclones generally develop prior to the development of the initial low-level mesocyclone (e.g., Burgess et al. 1982), as shown for a similar vertical cross section taken at 60 min in Fig. 19a. While the midlevel mesocyclone owes its existence to tilting and subsequent stretching of horizontal vorticity associated with the ambient vertical wind shear, low-level mesocyclones within supercell storms owe their existence largely to tilting and subsequent stretching of storm-generated horizontal vorticity associated with the surface outflow (e.g., Klemp 1987; Davies-Jones 1984; Rotunno and Klemp 1985).

As will be shown in Part II, the low-level mesovortices for the QLCS cases similarly depend on the development of downdraft and surface outflow, but, in contrast with supercell mesocyclones, they need not be associated with preexisting, quasi-steady rotating updrafts at mid- and upper-levels of the storm. These structural differences are more than cosmetic. They are, in fact, quite significant dynamically: midlevel rotating updrafts, which represent the key structural feature that makes supercells different from ordinary convection, are far more steady and vertically erect than the updrafts produced within the quasi-linear systems. Additionally, the strong dynamic pressure forcing associated with such midlevel rotating updrafts can produce far stronger vertical accelerations at low levels within the storm, accentuating the stretching potential for surface mesocyclones located beneath this updraft region (e.g., Weisman and Rotunno 2000). Such dynamic forcing is also responsible for the deviate propagation of supercell storms.

The differing characteristics of this dynamic forcing are elucidated for the present cases in Fig. 20, which presents the decomposition of the vertical acceleration in a representative cross section through the main updraft/mesocyclone region of the isolated supercell discussed above and mesovortex Vi from the $U_s = 30$ m s^{-1} over 5 km simulation at 4 h 20 min, at which time Vi is still associated with both significant updraft aloft and a significant hook feature in the rain field. Following Weisman and Rotunno (2000), the vertical acceleration is decomposed into total forcing (DWDT), dynamic forcing (PZDN), and buoyancy forcing (PZBY) via

$$\underbrace{\frac{dw}{dt}}_{\text{DWDT}} = \underbrace{-C_p\overline{\theta}_v\frac{\partial \pi_{\text{dn}}}{\partial z}}_{\text{PZDN}} + \underbrace{\left(-C_p\overline{\theta}_v\frac{\partial \pi_b}{\partial z} + B\right)}_{\text{PZBY}}, \quad (4.1)$$

where B is the full buoyancy, given by

$$B \equiv g\left[\frac{\theta'}{\overline{\theta}} + 0.61(q_v - \overline{q}_v) - q_c - q_r\right], \quad (4.2)$$

π is the Exner function, given by

$$\pi \equiv \left(\frac{p}{p_0}\right)^{R_d/C_p}, \quad (4.3)$$

and where $\pi = \pi_{\text{dn}} + \pi_B$ represents solutions to the following two Poisson equations:

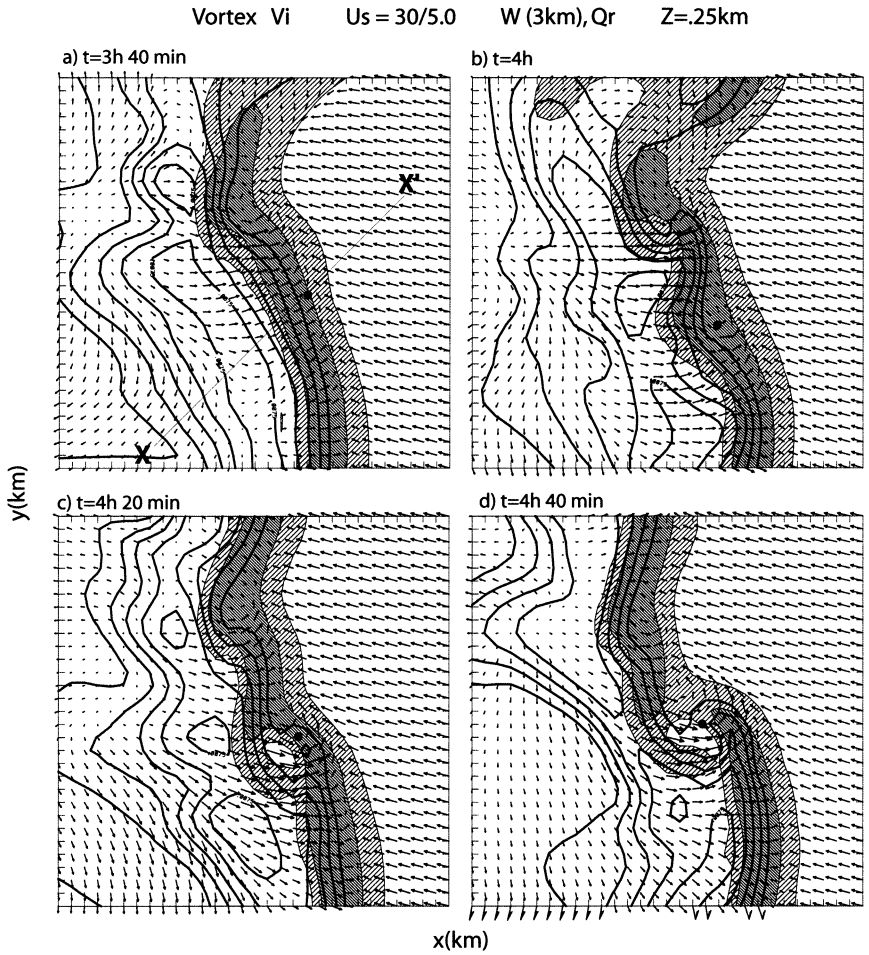

FIG. 14. Horizontal cross sections at 0.25 km AGL of system-relative flow and rain mixing ratio at (a) 3 h 40 min, (b) 4 h, (c) 4 h 20 min, and (d) 4 h 40 min for vortex Vi for the U_s = 30 m s^{-1} over 5 km shear simulation, as in Fig. 9. Bold dots indicate the location of vertical cross sections shown in Fig. 16.

$$\nabla \cdot (C_p \overline{\rho}\,\overline{\theta}_v \nabla \pi_{\rm dn}) = -\nabla \cdot (\overline{\rho}\mathbf{v} \cdot \nabla \mathbf{v}) \quad \text{and} \quad (4.4)$$

$$\nabla \cdot (C_p \overline{\rho}\,\overline{\theta}_v \nabla \pi_B) = \frac{\partial(\overline{\rho}B)}{\partial z}, \quad (4.5)$$

subject to the boundary conditions $\partial \pi_{\rm dn}/\partial z = 0$ and $\partial \pi_B/\partial z = B$ on $z = 0, h$.

Both storms show contributions from PZBY for the updraft at low-to-midlevels (Figs. 20c,f), as would be expected from the environmental thermodynamic profile (e.g., Fig. 3a). However, PZDN for the updrafts for the isolated supercell is fundamentally different than for the bow-echo updraft (e.g., Figs. 20b,e). Indeed, PZDN for the isolated supercell contributes significantly at midlevels of the storm, in association with the midlevel mesocyclone. In contrast, contributions from PZDN for the bow-echo updraft (Fig. 20f) are much weaker and are maximized near the surface, reflecting the strong convergence and rotation at the leading edge of the cold pool as opposed to forcing from a midlevel mesocyclone. Moreover, strong negative PZDN reflects in part the comparatively shallower, more tilted, and vertically diminishing character of the QLCS mesovortex. This further emphasizes that the dynamic structure of the mesovortices for these QLCS scenarios is quite distinct from that associated with supercell storms.

5. Summary and discussion

We have shown that significant, low-level cyclonic vortices are readily produced within the present idealized simulations of quasi-linear convective systems when the unidirectional environmental shear magnitude is U_s = 20 m s^{-1} or greater over the lowest 2.5–5 km AGL. In contrast to deeper, more erect mesovortices in these environments, much weaker, shallower, and shorter-lived vortices are produced for shear magnitudes of U_s = 15 m s^{-1} or less.

During the mature phase of the simulated QLCSs, the low-level mesovortices are found primarily north of the apex of individual embedded bowing segments, as well

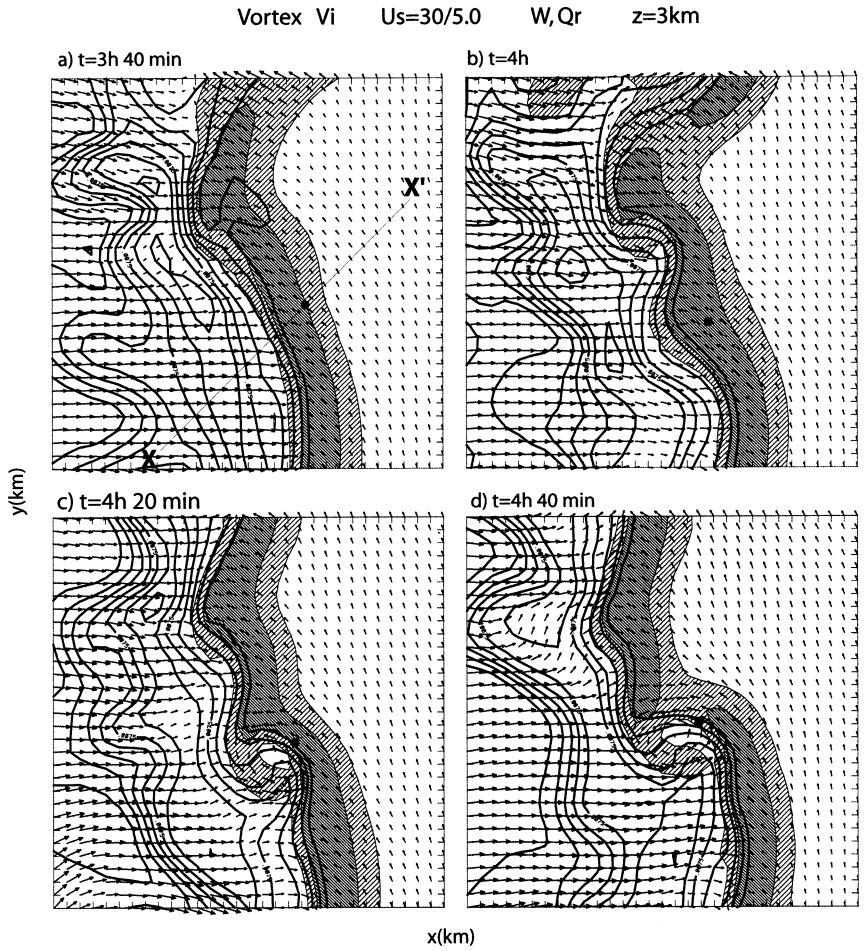

FIG. 15. Horizontal cross sections at 3 km AGL of system-relative flow updraft and rain mixing ratio at (a) 3 h 40 min, (b) 4 h, (c) 4 h 20 min, and (d) 4 h 40 min for vortex Vi for the U_s = 30 m s^{-1} over 5 km shear simulation, as in Fig. 9. Bold dots indicate the location of vertical cross sections shown in Fig. 16.

as north of the apex of the larger-scale bow-shaped system, and can have lifetimes of several hours, lasting far longer than individual convective cells. They are also often observed to merge and grow upscale over a several-hour period. The vortices generally develop first near the surface but can build upward to 6–8 km AGL, often resulting in a new midlevel line-end vortex. Indeed, the low-level vortices here develop independent of the midlevel line-end vortices described by Weisman (1993) and WD98. Also, while significant anticyclonic line-end vortices are readily produced at midlevels, significant anticyclonic vortices are not produced near the surface in these simulations. In Part II of this study we will discuss the mechanisms for vortex formation and, in particular, will establish that Coriolis forcing is critical for the production of such significant cyclonic low-level vortices.

The characteristics of these simulated mesovortices seem quite similar to those of observed mesovortices within QLCSs, including the predominance of cyclonic over anticyclonic low-level vortices, the observed north-of-apex bias, the upscale growth and merging of the vortices over time, as well as an association with especially large swaths of damaging surface winds (e.g., Fujita 1978; Wakimoto 1983; Smith and Partacz 1985; Przybylinski 1988; Przybylinski et al. 1996, 2000; Prost and Gerard 1997; Pence et al. 1998; Funk et al. 1996a,b; 1999; DeWald and Funk 2000; Miller and Johns 2000). In addition, the vertical wind shear environment necessary for the production of significant surface vortices within the idealized simulations (e.g., greater than 15 m s^{-1} of shear over the lowest 2–5 km AGL) matches well with the environments that have been associated with observed tornado-producing systems in the literature (e.g., Funk et al. 1999; DeWald and Funk 2000).

Although the present study does not explicitly address the association between such mesovortices and tornadoes, we are intrigued by the strong correspondence between the several long parallel paths of multiple tornadoes within the bow-echo system documented by

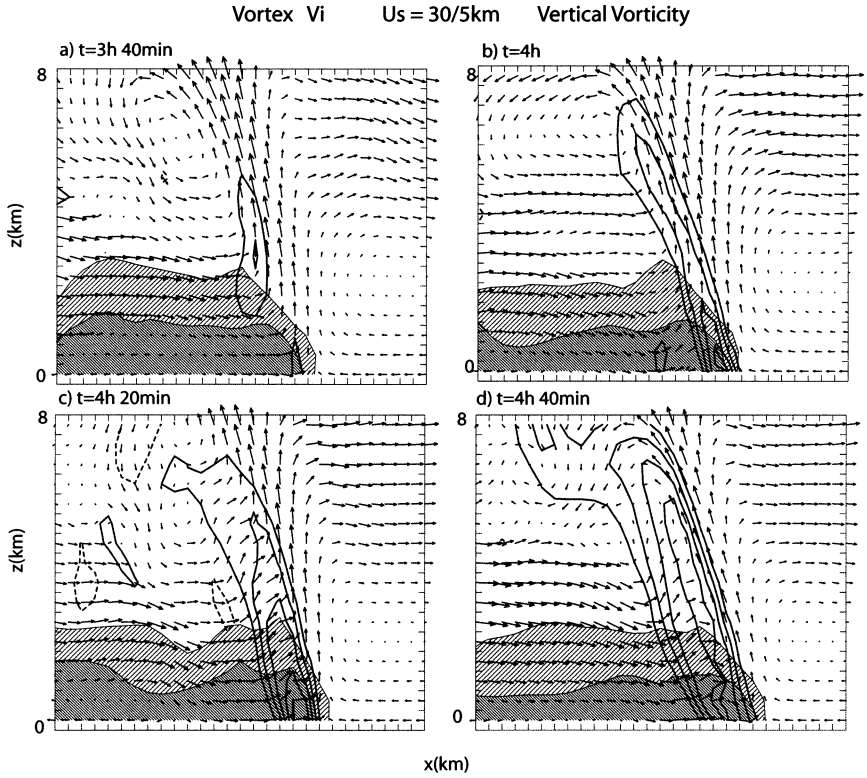

FIG. 16. Vertical cross sections of system-relative flow and vertical vorticity at (a) 3 h 40 min, (b) 4 h, (c) 4 h 20 min, and (d) 4 h 40 min, taken at a 45° angle through the low-level mesovortex, as indicated by the bold dots in Fig. 14, for vortex Vi for the $U_s = 20$ m s^{-1} over 2.5 km shear simulation, as in Fig. 11.

Forbes and Wakimoto (1983; Fig. 1) and the long, parallel mesovortex paths highlighted in the present simulations (e.g., Figs. 8 and 13). This observed case also offers some evidence of vortex merging, resulting in stronger tornadoes over time. Unfortunately, neither this study nor even the more recent observational studies of such mesovortices possesses the information needed for a detailed comparison with our idealized simulations. It is hoped that the upcoming Bow Echo and Mesoscale Convective Vortex (MCV) Experiment (BAMEX; Davis et al. 2001), scheduled for the spring of 2003, will offer such observations, thus allowing for a more systematic comparison with the simulation results.

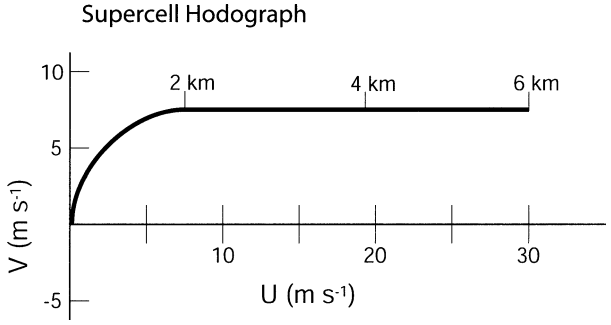

FIG. 17. Hodograph used for isolated supercell simulation, as described in the text.

Both the low-level and midlevel cyclonic vortices produced in these simulations have strengths comparable to supercell mesocyclones, although the mesovortex sizes are often much larger than mesocyclones at later stages in their life cycle. In addition, mesovortices can be associated with hook structures in the rain field. However, it is important to reemphasize that, although supercells can be embedded within organizied QLCSs, the mesovortices described here are not associated with supercells. In particular, there is no long-lived, rotating updraft above the low-level vortices (although they can be associated with updraft aloft at early stages), and the vortices do not propagate significantly differently from the mean wind. Thus, caution must be taken in assuming that low-level and midlevel mesovortices embedded within severe QLCSs must necessarily be supercellular in character.

The apparent differences between supercell mesocyclones and the present mesovortices also have important forecasting implications, especially for the use of storm-relative environmental helicity (SREH; e.g., Davies-Jones 1984), which is commonly used to anticipate supercell mesocyclone potential. For supercells, large magnitudes of SREH are realized in strongly

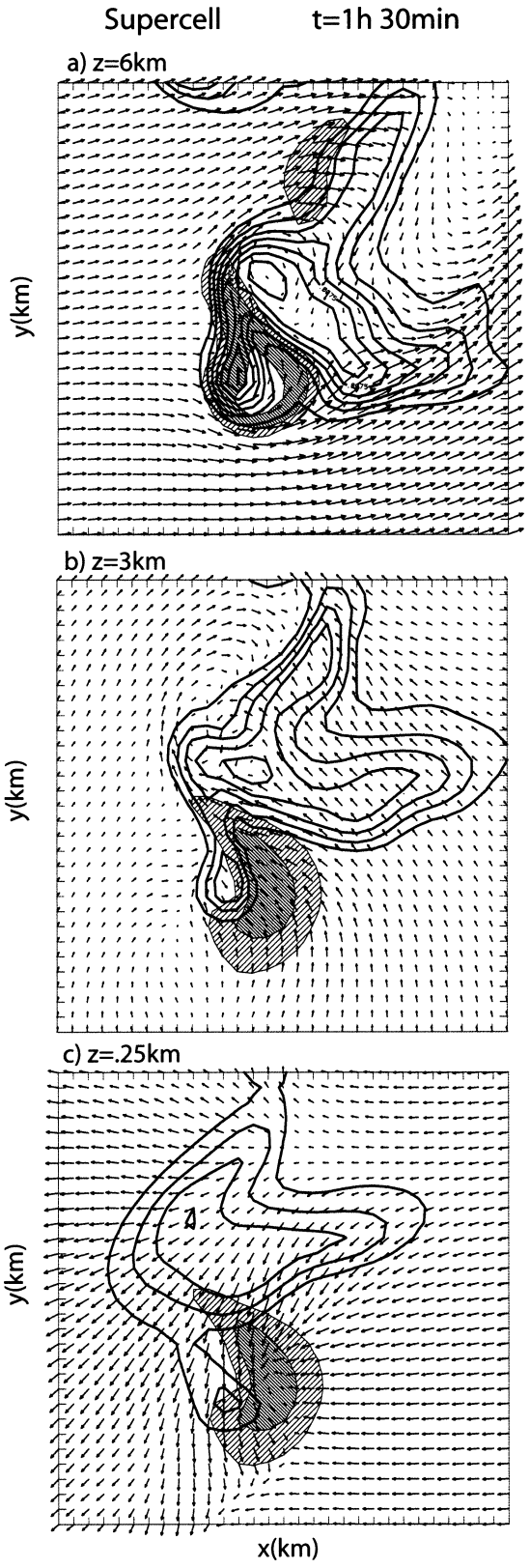

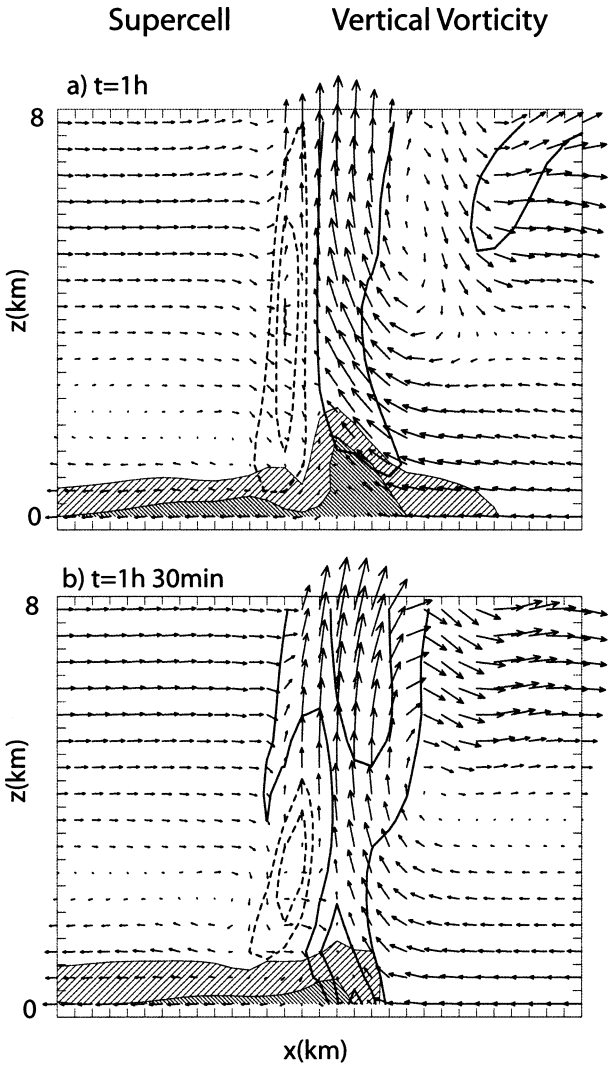

FIG. 19. Vertical cross sections of system-relative flow and vertical vorticity at (a) 1 h and (b) 1 h 40 min taken at a 90° angle through the surface vortex, as shown in Fig. 18, for the $U_s = 35$ m s^{-1} over 6 km 1/4 circle shear supercell simulation. Vorticity is contoured using a 40×10^{-4} s^{-1} interval, as in Fig. 11.

←

FIG. 18. Horizontal cross sections of system-relative flow, updraft, and rain mixing ratio at (a) 6, (b) 3, and (c) 0.25 km AGL for the $U_s = 35$ m s^{-1} over 6 km 1/4 circle shear supercell simulation at 1 h 40 min, as described in the text. Updraft is lightly hatched for magnitudes between 4 and 12 m s^{-1}, darkly hatched for magnitudes between 12 and 30 m s^{-1}, and unhatched for magnitudes greater than 30 m s^{-1}. In (c), updraft is presented at 3 km rather than 0.25 km AGL to clarify the association between the low-level mesovortex and the location of updraft aloft. Rain mixing ratio is contoured using a 0.0015 g kg^{-1} interval. Vectors are included every grid point, with a vector length of one grid point equal to a wind magnitude of 20 m s^{-1}. Tick marks are included every kilometer. Only a 30 km by 30 km portion of the full domain is shown.

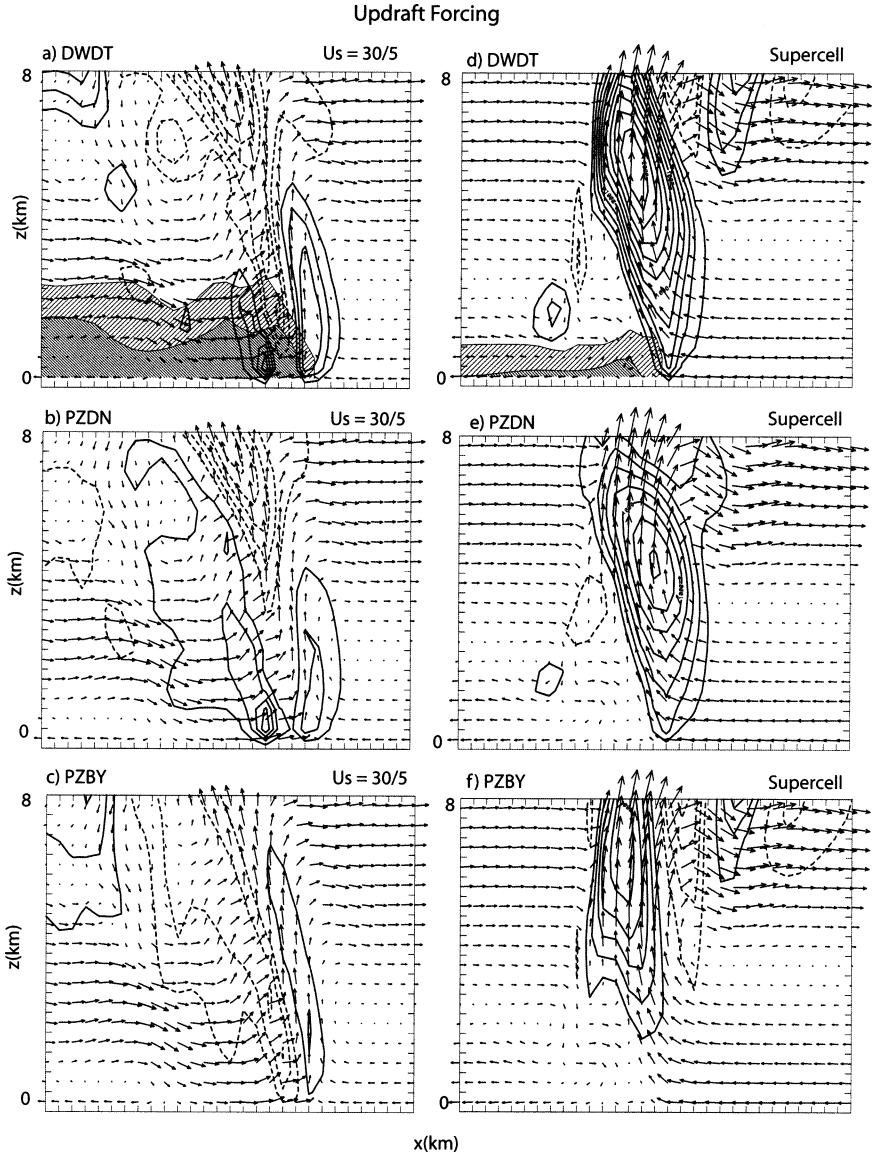

FIG. 20. Total vertical velocity forcing (DWDT), dynamic forcing (PZDN), and buoyant forcing (PZBY) for (a), (b), (c) vortex Vi for the $U_s = 30$ m s^{-1} over 5 km QLCS simulation and (d), (e), (f) the isolated supercell simulation, respectively, as described in the text. Forcing terms are contoured using a 0.002 m s^{-2} interval, with the zero contour omitted. Vectors and shading are the same as in Fig. 11.

sheared environments when storm motion deviates significantly off the hodograph, reflecting a large amount of environmental streamwise vorticity that could potentially be tilted within the storm's updraft to produce a mesocyclone. However, the mesovortices studied in the present paper do not exhibit such significant off-hodograph propagation, implying that descriptions based on streamwise vorticity are not applicable to these phenomena. Indeed, both midlevel (WD98) and low-level (see Part II) mesovortices are generated in the present idealized simulations via the tilting of crosswise rather than streamwise vorticity. Thus, the concept of SREH does not appear relevant to the prediction of these mesovortices, at least based on these idealized simulations. The present results, however, do suggest that the potential for mesovortex formation within a QLCS can be anticipated without regard to cell or vortex motion when the environment is especially characterized by strong, low-level vertical wind shear.

Based on our own and closely related sensitivity studies (e.g., Atkins and Arnott 2002), we are confident that the basic results presented herein are robust. Yet, we should reemphasize that the present simulation results apply strictly to a single thermodynamic profile of mod-

erate instability with deep moisture and unidirectional vertical wind shear. Future studies will need to consider sensitivities to these as well as many other environmental and numerical-model parameters. For instance, low-level hodograph curvature has been shown to contribute significantly to the production of supercell mesocyclones (e.g., Wicker 1996). Adlerman and Droegemeier (2002) show that the details of cyclic mesocyclogenesis within supercell storms can be very sensitive to vertical and horizontal grid resolution, physical and numerical mixing, and surface drag, as well as choice of microphysical parameterizations. The present simulations also only consider mechanisms internal to the convective system itself (e.g., the systems evolve in horizontally homogeneous conditions). Many recent studies, however, have emphasized the potential role of preexisting boundaries (e.g., Schmocker et al. 2000) or other mesoscale variability (e.g., Coniglio and Stensrud 2001) on the evolution of such systems. Future studies will thus also need to consider the sensitivity of system structure to the existence of such preexisting mesoscale features.

Acknowledgments. Comments on both Parts I and II by H. Bluestein, C. Davis, D. Dowell, and three anonymous reviewers helped improve our presentations significantly. Funding for RJT was provided in part under NOAA–OU Cooperative Agreement NA17RJ1227 and in part by the National Science Foundation under NSF Grant ATM-0100016.

REFERENCES

Adlerman, E. J., and K. K. Droegemeier, 2002: Sensitivity of numerically simulated cyclic mesocyclogenesis to variations in model physical and computational parameters. *Mon. Wea. Rev.*, **130,** 2671–2691.

Atkins, N. T., and J. M. Arnott, 2002: Tornadogenesis within quasilinear convective systems. Part II: Preliminary WRF simulation results of the 29 June 1998 derecho. Preprints, *21st Conf. on Severe Local Storms,* San Antonio, TX, Amer. Meteor. Soc., 498–501.

Bernardet, L. R., and W. R. Cotton, 1998: Multiscale evolution of a derecho-producing mesoscale convective system. *Mon. Wea. Rev.,* **126,** 2991–3015.

Bluestein, H., and M. L. Weisman, 2000: The interaction of numerically simulated supercells initiated along lines. *Mon. Wea. Rev.*, **128,** 3128–3149.

Burgess, D. W., and B. F. Smull, 1990: Doppler radar observations of a bow echo associated with a long-track severe windstorm. Preprints, *16th Conf. on Severe Local Storms,* Kananaskis Park, AB, Canada, Amer. Meteor. Soc., 203–208.

——, V. T. Wood, and R. A. Brown, 1982: Mesocyclone evolution statistics. Preprints, *12th Conf. on Severe Local Storms,* San Antonio, TX, Amer. Meteor. Soc., 422–424.

Coniglio, M. C., and D. J. Stensrud, 2001: Simulation of a progressive derecho using composite initial conditions. *Mon. Wea. Rev.*, **129,** 1593–1616.

Davies-Jones, R. P., 1984: Streamwise vorticity: The origin of updraft rotation in supercell storms. *J. Atmos. Sci.,* **41,** 2991–3006.

Davis, C. A., and M. L. Weisman, 1994: Balanced dynamics of mesoscale vortices produced in simulated convective systems. *J. Atmos. Sci.,* **51,** 2005–2030.

——, and Coauthors, cited 2001: Science overview of the bow echo and MCV experiment (BAMEX). [Available online at http://www.mmm.ucar.edu/bamex/science.html.]

DeWald, V. L., and T. W. Funk, 2000: WSR-88D reflectivity and velocity trends of a damaging squall line event on 20 April 1996 over south-central Indiana and central Kentucky. Preprints, *20th Conf. on Severe Local Storms,* Orlando, FL, Amer. Meteor. Soc., 177–180.

Evans, J. S., and C. A. Doswell III, 2001: Examination of derecho environments using proximity soundings. *Wea. Forecasting,* **16,** 329–342.

Forbes, G. S., and R. M. Wakimoto, 1983: A concentrated outbreak of tornadoes, downbursts and microbursts, and implications regarding vortex classification. *Mon. Wea. Rev.,* **111,** 220–235.

Fujita, T. T., 1978: Manual of downburst identification for project NIMROD. Satellite and Mesometeorology Research Paper 156, Dept. of Geophysical Sciences, University of Chicago, 104 pp.

——, 1981: Tornadoes and downbursts in the context of generalized planetary scales. *J. Atmos. Sci.,* **38,** 1511–1524.

Funk, T. W., K. E. Darmofal, J. D. Kirkpatrick, M. T. Shields, R. W. Przybylinski, Y.-J Lin, G. K. Schmocker, and T. J. Shea, 1996a: Storm reflectivity and mesocyclone evolution associated with the 15 April 1994 Derecho. Part II: Storm structure and evolution over Kentucky and southern Indiana. Preprints, *18th Conf. on Severe Local Storms,* San Franscisco, CA, Amer. Meteor. Soc., 516–520.

——, B. F. Smull, and J. D. Ammerman, 1996b: Structure and evolution of an intense bow echo embedded within a heavy rain producing MCS over Missouri. Preprints, *18th Conf. on Severe Local Storms,* San Franscisco, CA, Amer. Meteor. Soc., 521–526.

——, K. E. Darmofal, J. D. Kirkpatrick, V. L. Dewald, R. W. Przybylinski, G. K. Schmocker, and Y.-J Lin, 1999: Storm reflectivity and mesocyclone evolution associated with the 15 April 1994 squall line over Kentucky and southern Indiana. *Wea. Forecasting,* **14,** 976–993.

Johns, R. H., and W. D. Hirt, 1987: Derechos: Widespread convectively induced windstorms. *Wea. Forecasting,* **2,** 32–49.

Jorgensen, D. P., and B. F. Smull, 1993: Mesovortex circulations seen by airborne Doppler radar within a bow-echo mesoscale convective system. *Bull. Amer. Meteor. Soc.,* **74,** 2146–2157.

Klemp, J. B., 1987: Dynamics of tornadic thunderstorms. *Annu. Rev. Fluid Mech.,* **19,** 369–402.

——, and R. B. Wilhelmson, 1978: The simulation of three-dimensional convective storm dynamics. *J. Atmos. Sci.,* **35,** 1070–1096.

Lafore, J., and M. W. Moncrieff, 1989: A numerical investigation of the organization and interaction of the convective and stratiform regions of tropical squall lines. *J. Atmos. Sci.,* **46,** 521–544.

Lee, B. D., and R. B. Wilhelmson, 1997: The numerical simulation of non-supercell tornadogenesis. Part I: Initiation and evolution of pretornadic misocyclone and circulations along a dry outflow boundary. *J. Atmos. Sci.,* **54,** 32–60.

McWilliams, J. C., 1984: The emergence of isolated coherent vortices in turbulent flow. *J. Fluid. Mech.,* **146,** 21–43.

Miller, D. J., and R. H. Johns, 2000: A detailed look at extreme wind damage in derecho events. Preprints, *20th Conf. on Severe Local Storms,* Orlando, FL, Amer. Meteor. Soc., 52–55.

Moller, A. R., C. A. Doswell III, M. P. Foster, and G. R. Woodall, 1994: The operational recognition of supercell thunderstorm environments and storm structures. *Wea. Forecasting,* **9,** 327–347.

Pence, K. J., J. T. Bradshaw, and M. W. Rose, 1998: The central Alabama tornadoes of 6 March 1996. Preprints, *19th Conf. on Severe Local Storms,* Minneapolis, MN, Amer. Meteor. Soc., 147–154.

Prost, R. L., and A. E. Gerard, 1997: ''Bookend vortex'' induced tornadoes along the Natchez Trace. *Wea. Forecasting,* **12,** 572–580.

Przybylinski, R. W., 1988: Radar signatures with the 10 March 1986 tornado outbreak over central Indiana. Preprints, *15th Conf. on*

Severe Local Storms, Baltimore, MD, Amer. Meteor. Soc., 253–256.

——, 1995: The bow echo: Observations, numerical simulations, and severe weather detection methods. *Wea. Forecasting,* **10,** 203–218.

——, and D. M. DeCaire, 1985: Radar signatures associated with the derecho, a type of mesoscale convective system. Preprints, *14th Conf. on Severe Local Storms,* Indianapolis, IN, Amer. Meteor. Soc., 228–231.

——, and Coauthors, 1996: Storm reflectivity and mesocyclone evolution associated with the 15 April 1994 derecho. Part I: Storm evolution over Missouri and Illinois. Preprints, *18th Conf. on Severe Local Storms,* San Franscisco, CA, Amer. Meteor. Soc., 509–515.

——, G. K. Schmocker, and Y.-J. Lin, 2000: A study of storm and vortex morphology during the ''intensifying stage'' of severe wind mesoscale convective systems. Preprints, *20th Conf. on Severe Local Storms,* Orlando, FL, Amer. Meteor. Soc., 173–176.

Rotunno, R., and J. B. Klemp, 1985: On the rotation and propagation of simulated supercell thunderstorms. *J. Atmos. Sci.,* **42,** 271–292.

——, ——, and M. L. Weisman, 1988: A theory for strong, long-lived squall lines. *J. Atmos. Sci.,* **45,** 463–485.

Schmidt, J. M., and W. R. Cotton, 1989: A High Plains squall line associated with severe surface winds. *J. Atmos. Sci.,* **46,** 281–302.

Schmocker, G. K., R. W. Przybylinski, and E. N. Rasmussen, 2000: The severe bow echo event of 14 June 1998 over the mid-Mississippi valley region: A case of vortex development near the intersection of a preexisting boundary and a convective line. Preprints, *20th Conf. on Severe Local Storms,* Orlando, FL, Amer. Meteor. Soc., 169–172.

Skamarock, W. C., M. L. Weisman, and J. B. Klemp, 1994: Three-dimensional evolution of simulated long-lived squall lines. *J. Atmos. Sci.,* **51,** 2563–2584.

Smith, B. E., and J. W. Partacz, 1985: Bow-echo induced tornado at Minneapolis on 26 April 1984. Preprints, *14th Conf. on Severe Local Storms,* Indianapolis, IN, Amer. Meteor. Soc., 81–84.

Smull, B. F., and R. A. Houze Jr., 1987: Rear inflow in squall lines with trailing stratiform precipitation. *Mon. Wea. Rev.,* **115,** 2869–2889.

Tessendorf, S. A., and R. J. Trapp, 2000: On the climatological distribution of tornadoes within quasi-linear convective systems. Preprints, *20th Conf. on Severe Local Storms,* Orlando, FL, Amer. Meteor. Soc., 134–137.

Trapp, R. J., and M. L. Weisman, 2003: Low-level mesovortices within squall lines and bow echoes. Part II: Their genesis and implications. *Mon. Wea. Rev.,* **131,** 2804–2817.

——, E. D. Mitchell, G. A. Tipton, D. W. Effertz, A. I. Watson, D. L. Andra Jr., and M. A. Magsig, 1999: Descending and nondescending tornadic vortex signatures detected by WSR-88Ds. *Wea. Forecasting,* **14,** 625–639.

Wakimoto, R. M., 1983: The West Bend, Wisconsin storm of 4 April 1981: A problem in operational meteorology. *J. Climate Appl. Meteor.,* **22,** 181–189.

Weisman, M. L., 1992: The role of convectively generated rear-inflow jets in the evolution of long-lived mesoconvective systems. *J. Atmos. Sci.,* **49,** 1826–1847.

——, 1993: The genesis of severe, long-lived bow-echoes. *J. Atmos. Sci.,* **50,** 645–670.

——, and J. B. Klemp, 1982: The dependence of numerically simulated convective storms on vertical wind shear and buoyancy. *Mon. Wea. Rev.,* **110,** 504–520.

——, and ——, 1984: The structure and classification of numerically simulated convective storms in directionally varying wind shears. *Mon. Wea. Rev.,* **112,** 2479–2498.

——, and ——, 1986: Characteristics of isolated convective storms. *Mesoscale Meteorology and Forecasting,* P. S. Ray, Ed., Amer. Meteor. Soc., 331–358.

——, and C. Davis, 1998: Mechanisms for the generation of mesoscale vortices within quasi-linear convective systems. *J. Atmos. Sci.,* **55,** 2603–2622.

——, and R. Rotunno, 2000: The use of vertical wind shear versus helicity in interpreting supercell dynamics. *J. Atmos. Sci.,* **57,** 1452–1472.

——, J. B. Klemp, and R. Rotunno, 1988: Structure and evolution of numerically simulated squall lines. *J. Atmos. Sci.,* **45,** 1990–2013.

Wicker, L. J., 1996: The role of near-surface wind shear on low-level mesocyclone generation and tornadoes. Preprints, *18th Conf. on Severe Local Storms,* San Franscisco, CA, Amer. Meteor. Soc., 115–119.